universität wien

MASTERARBEIT | MASTER'S THESIS

Titel | Title

The Influence of Wind Speed and Sea Surface Temperature on Sea Spray Aerosol Concentration during the AEROMMA Campaign

verfasst von | submitted by

Sophie Katharina Scharinger BSc

angestrebter akademischer Grad | in partial fulfilment of the requirements for the degree of

Master of Science (MSc)

Wien | Vienna, 2025

Studienkennzahl lt. Studienblatt | Degree programme code as it appears on the student record sheet:	UA 066 876
Studienrichtung lt. Studienblatt | Degree programme as it appears on the student record sheet:	Masterstudium Physics
Betreut von | Supervisor:	Univ.-Prof. Dr. Bernadett Weinzierl
Mitbetreut von | Co-Supervisor:	Dipl.-Ing. Dr. Agnieszka Straus BSc MSc

Abstract

Sea spray aerosol (SSA), aerosol of any composition emitted as droplets at the ocean surface, accounts for about 70% to the total aerosol mass emitted into the atmosphere every year. SSA is responsible for the majority of scattering in the marine atmosphere and contributes significantly to the cloud condensation nuclei population over the remote ocean. Consequently, understanding the abundance and properties of SSA is critical in order to quantify the effect that aerosols have on our climate. The main known parameters for SSA production are wind speed and sea surface temperature (SST). However, the effect of wind speed and SST on SSA concentration, size distribution and properties are not yet well constrained.

The aircraft-based Atmospheric Emissions and Reactions Observed from Megacities to Marine Areas (AEROMMA) campaign was conducted onboard the NASA DC-8 aircraft between May and August 2023 out of Palmdale, California and Dayton, Ohio. Four research flights of this campaign, which took place between June 16th and June 23rd, sampled the marine boundary layer above the Pacific Ocean off the coast of California. This thesis analyzes aerosol measurements acquired during the marine flights of the AEROMMA campaign, focusing on SSA and its dependence on wind speeds up to 31 m/s and sea surface temperatures between 283 and 295 K. The primary data source for this thesis is the University of Vienna's Cloud, Aerosol, and Precipitation Spectrometer (UNIVIE-CAPS), which was installed under the wingtip of the NASA DC-8 research aircraft and measured aerosol particles between 0.5 and 930 µm. Data on sea surface temperature was provided by the Scanning High-resolution Interferometer Sounder (S-HIS). Furthermore, size-resolved particle composition data in an ambient diameter range of 0.5–4 µm from the Particle Analysis by Laser Mass Spectrometry (PALMS) instrument was used in the analysis.

Results show that the aerosol particles with ambient diameters between 1.5 and 4 µm measured in the marine boundary layer were mostly sea salt, which is the primary component of SSA. In contrast, the aerosol composition in the size range of 0.5–1.5 µm was influenced significantly by biomass burning and sulfate, organic and nitrate particles. Based on previous studies, an increase in SSA concentration with increasing wind speed and increasing SST is expected. While the amount of SSA particles measured falls into the broad range reported in literature and is higher at wind speeds > 10 m/s than at windspeeds < 10 m/s, it shows no consistent positive dependence on wind speeds. The increased SSA number concentrations at wind speeds above 10 m/s are also reflected in the total particle number size distribution. No effect of SST on SSA concentrations could be identified in this study, which may partly be due to a narrow range of SST which only varied between 283 and 295 K. During one flight, an unexpected decrease in SSA number concentration with wind speed was observed. Back

trajectories calculated with the HYSPLIT model indicate that the measurements during that period were sampled at the boundary between two distinct airmasses.

Kurzfassung

Sea Spray Aerosol (SSA), Aerosol jeglicher Zusammensetzung das als Tröpfchen an der Meeresoberfläche emittiert wird, bildet der Masse nach das meist-emittierte Aerosol in unserer Atmosphäre. SSA ist verantwortlich für den Großteil der Strahlungsstreuung in der marinen Atmosphäre und trägt maßgeblich zur Population von Wolkenkondensationskernen über abgelegenen Meeresgebieten bei. Folglich ist das Verständnis der Menge und Eigenschaften von SSA von entscheidender Bedeutung, um die Auswirkungen von Aerosolen auf unser Klima zu quantifizieren. Die wichtigsten bekannten Parameter von SSA Produktion sind Windgeschwindigkeit und die Temperatur der Meeresoberfläche. Allerdings sind die Auswirkungen von Windgeschwindigkeit und Meeresoberflächentemperatur auf SSA Konzentration, Größenverteilung und Eigenschaften noch nicht vollständig erforscht.

Die Flugzeuggestützte ‚Atmospheric Emissions and Reactions Observed from Megacities to Marine Areas' (AEROMMA) Kampagne wurde zwischen Mai und August 2023 an Bord des NASA DC-8 Flugzeugs durchgeführt. Vier Forschungsflüge dieser Kampagne, die zwischen 16. und 23. Juni geflogen wurden, dienten der Erforschung der marinen Grenzschicht über dem Pazifik vor der kalifornischen Küste. Die vorliegende Masterarbeit befasst sich mit Aerosolmessungen in der marinen Grenzschicht während dieser marinen Flüge, wobei der Schwerpunkt auf SSA und seiner Abhängigkeit von Windgeschwindigkeiten bis zu 31 m/s und Meeresoberflächentemperaturen zwischen 283 und 295 K liegt. Die primäre Datenquelle für diese Arbeit ist das ‚Cloud, Aerosol, and Precipitation Spectrometer' der Universität Wien (UNIVIE-CAPS), welches unter der Flügelspitze des NASA DC-8 Flugzeugs installiert war und Aerosolpartikel mit Durchmessern zwischen 0.5 und 930 µm gemessen hat. Die Meeresoberflächentemperature wurde vom ‚Scanning High-resolution Interferometer Sounder' (S-HIS) gemessen und bereitgestellt. Weiters wurden Daten zur chemischen Zusammensetzung von Aerosolpartikeln mit Durchmessern zwischen 0.5 und 4 µm analysiert, die vom ‚Particle Analysis by Laser Mass Spectrometry' (PALMS) Instrument aufgezeichnet wurden.

Die Ergebnisse zeigen, dass Aerosolpartikel mit Durchmessern zwischen 1.5 und 4 µm in der marinen Grenzschicht überwiegend aus Seesalz, der Hauptkomponente von SSA, bestehen. Die Zusammensetzung von Aerosolpartikel im Größenbereich von 0.5–1.5 µm hingegen wurde signifikant beeinflusst von Partikeln aus Biomasseverbrennung und organischen sowie Sulfat- und Nitratpartikeln. Basierend auf vorangegangenen Studien wurde ein Anstieg an SSA Anzahlkonzentration mit steigender Windgeschwindigkeit und Meeresoberflächentemperatur erwartet. Die gemessene Anzahlkonzentration von SSA fällt in die Bandbreite, welche die Fachliteratur angibt. Bei Windgeschwindigkeiten > 10 m/s ist die SSA Anzahlkonzentration

höher als bei Windgeschwindigkeiten < 10 m/s, allerdings zeigt sie keine konsistente positive Abhängigkeit von Windgeschwindigkeit. Die erhöhten Anzahlkonzentrationen bei Windgeschwindigkeiten > 10 m/s sind auch in den Größenverteilungen erkennbar. Weiters wurde kein Effekt von Meeresoberflächentemperatur auf die SSA Anzahlkonzentration festgestellt, was möglicherweise zum Teil der geringen Variation von Meeresoberflächentemperatur während der Messungen zuzuschreiben ist, die zwischen 283 und 295 K schwankte. Bei einem der Forschungsflüge wurde eine unerwartete Reduktion von SSA Anzahlkonzentration mit steigender Windgeschwindigkeit beobachtet. Mit dem HYSPLIT-Modell berechnete Trajektorien indizieren, dass die betreffenden Daten an einer Grenzschicht zwischen zwei unterschiedlichen Luftmassen gemessen wurde.

Acknowledgements

I would like to express my deepest gratitude to my supervisor Bernadett Weinzierl for the opportunity to write my master's thesis in the aerosol physics group and to participate in the AEROMMA project. Thank you for your guidance! Special thanks also to my co-supervisor Agnieszka Straus, for her much-needed support and feedback and to Maximilian Dollner, for taking the time to answer all my questions regarding the CAPS instrument.

Many thanks also go to Xiaoli Shen and the PALMS team for providing the data on aerosol composition for this work, as well as answering all of my questions.

Furthermore, I'm grateful for the all the support I received from the aerosol physics group. Thank you all for the warm welcome, the enjoyable lunch breaks and the interesting discussions. In particular, thank you Mirjam and Florian! I will miss our office talks.

Lastly, thank you to Bruno and my family, without whom none of this would have been possible. Your encouragement has carried me through this journey.

Table of Contents

Abstract III
Kurzfassung V
Acknowledgements VII
1. Introduction 1
2. Theoretical Background 5
2.1. Aerosol Particle Size 5
2.2. Aerosol Optical Properties 7
2.3. Global Aerosol Burden and Effects 7
2.3.1. Sources and Removal 7
2.3.2. Distribution 9
2.4. Sea Spray Aerosol 10
2.4.1. Production Mechanisms 10
2.4.2. Properties 12
3. Methods 13
3.1. The AEROMMA Campaign 13
3.2. Instrumentation: The UNIVIE-CAPS 14
3.2.1. Working Principle 14
3.2.2. CAS Calibration 15
3.3. Other Instruments 16
3.4. HYSPLIT 18
3.5. Data Selection and Processing 19
4. Results 23
4.1. Data Selection 23
4.2. Ambient Conditions and Aerosol Composition 25
4.3. Number Concentration 28
4.3.1. Dependence on Wind Speed 28
4.3.2. Dependence on Sea Surface Temperature 30
4.4. Number Size Distribution 31
5. Discussion 34
5.1. General Findings 34
5.2. Case Study 42
6. Conclusions 48
Bibliography 50
Appendix 61

1. Introduction

Aerosols affect our climate by various pathways, which can be grouped into two main kinds of interaction and are well-described in Boucher (2015) and Lohmann et al. (2016): *Aerosol-radiation interactions (ari)* describe the processes in which aerosols effectively change the reflectivity, or *albedo* of the earth (Boucher, 2015; Seinfeld & Pandis, 1998). Whether an aerosol species has an overall warming or cooling effect on our atmosphere is dependent on how much it absorbs/scatters and on the properties of the planetary surface below it. For example, a layer of SSA above the ocean has a cooling effect, because particles containing sea salt, the main component of SSA, scatter more light than the ocean surface (Boucher, 2015). *Aerosol-Cloud interactions (aci),* on the other hand, affect our climate by modifying cloud properties (Boucher, 2015). Through their role as so-called cloud condensation nuclei (CCN) and ice nucleating particles (INPs), aerosol particles lead to an increase in the number of cloud droplets. This abundance of CCN/INPs results in a decrease in droplet size and increase in reflectivity of the cloud, and thus in a higher albedo and cooling effect. It also can prolong the lifetime of clouds and lead to cloud glaciation (Lohmann et al., 2016)

The effect of these interactions can be quantified using radiative forcing (RF), which is a change in radiative flux at the top of the atmosphere in response to a perturbation and is quantified in W/m^2. The radiative forcing of the two categories of aerosol-climate effects are also referred to as RFari and RFaci (Lohmann et al., 2016). Even though both types of aerosol-climate effects are poorly constrained, it is agreed upon that in the global mean, they have been exerting a cooling effect on our climate since 1750. The Fifth Assessment Report of the Intergovernmental Panel on Climate Change (IPCC) reports the effective radiative forcing (ERF), which is the RF including rapid adjustments such as surface warming, changes in atmospheric profiles and cloudiness. The anthropogenic ERF of aerosol-radiation interactions and aerosol-cloud interactions are estimated as $-0.9\ W/m^2$ with a 5% to 95% uncertainty range of -1.9 to $-0.1\ W/m^2$ (Boucher et al., 2013). While the effects of aerosol on our climate are still a major topic of discussion within the scientific community, the understanding has increased drastically within the last decade. However, the Fifth Assessment Report of the IPCC still labels the confidence in current estimates only as ‘medium’ for the total aerosol effect. This is a combination of a ‘high’ confidence in aerosol radiation interactions and a ‘low’ confidence in aerosol-cloud interactions and rapid adjustment aerosol-radiation interaction (Myhre et al., 2013). Additional research is needed to further constrain the effects of aerosols on earth’s climate. This thesis aims to contribute to the scientific discourse by investigating sea spray aerosol (SSA), i.e. particles of ocean water emitted at the sea surface.

It is known that by mass, sea salt is the most abundantly emitted aerosol type (Dentener et al., 2006). However, of all aerosol species, it also exhibits the largest uncertainty in mass (Grythe et al., 2014). As mentioned previously, sea salt particles reflect more electromagnetic radiation than the ocean surface, which leads to negative RFari exerted by sea spray aerosol. Estimates of the global all-sky RFari, i.e. the RFari in both clear and cloudy conditions, of sea spray aerosol range between −0.3 and −1.1 W/m^2 (Grini et al., 2002; Koch et al., 2006; Liao et al., 2004; Ma et al., 2008; Reddy et al., 2005). Thus, while studies do agree that the global RFari of sea spray aerosol is negative, there is a significant variation of 0.8 W/m^2. Additionally, SSA particles exhibit a high hygroscopicity and readily act as CCN (Forestieri et al., 2018; O'Dowd et al., 2004). A supersaturation of only 0.1% is enough to activate SSA particle with diameters ≥0.2 µm (diameter at 80% RH) as CCN (Lewis & Schwartz, 2004). Their contribution to the global all-sky RFaci has been estimated as −1.34 W/m^2 and even −2.9 W/m^2 including climatic feedbacks (Ma et al., 2008). SSA particles furthermore act as sinks for reactive atmospheric gases and contribute to the depletion of ozone through the production of reactive halogen species, specifically chlorine and bromine (Simpson et al., 2015; Zhu et al., 2019).

Improving our understanding of the production mechanisms of sea spray aerosol is one of the most important tasks to understand pre-industrial aerosol abundance and composition, as well as historical climate, which serves as a reference period for future projections (Carslaw et al., 2017). Furthermore, the abundance and properties SSA will likely be affected by climate change: A warming climate leads to melting of sea ice, which results in more open water and a smaller average roughness length, a measure that describes the surface roughness and is defined as the height above the surface at which the wind is zero (Boucher, 2015; Stull, 1988). A decrease in roughness length may result in an increase in surface wind speed (Boucher, 2015). In turn, these two factors lead to an increased production of SSA (Boucher, 2015). Further changes in global near-surface wind speeds, rising water temperatures and decreasing salinity due to glacier melting may also affect SSA production (Liu et al., 2021; Mårtensson et al., 2003; Zha et al., 2021). On the other hand, the effect of increased SSA concentrations on the planetary albedo needs to be taken into account when studying future climate (Winter & Chýlek, 1997).

There are several production mechanisms of SSA, described in detail in Section 2.4.1, which are mostly associated with wave breaking. Since wave breaking is wind-driven, the main parameter controlling the production of SSA particles is wind speed (Lewis & Schwartz, 2004), which generates shear stress on the ocean surface and results in waves. Although Grythe et al. (2014) recommends using shear stress to parametrize the whitecap fraction and SSA production, most of the available literature uses wind speed at 10 m above the ocean surface

as a proxy, which exhibits significant spatial and temporal variability. Several studies report a positive correlation between wind speed and measured SSA concentrations (Feng et al., 2017; Jaeglé et al., 2011; Liu et al., 2021; Saliba et al., 2019; Zheng et al., 2018) The details of the SSA – wind speed relationship beyond this remain disputed and not yet well understood. Furthermore, the range of wind speed values reported is rather constrained: Most studies that report a relationship between SSA concentrations and wind speed present measurements of wind speeds only up to 15–20 m/s (Feng et al., 2017; Jaeglé et al., 2011; Liu et al., 2021; Zheng et al., 2018). The few studies that measured wind speeds greater than 20 m/s have found a continued increase of SSA concentrations with increasing wind speed (Saliba et al., 2019), a levelling off (Bruch et al., 2023) and even a decrease (Pant et al., 2008). Consequently, more data is needed on high wind speed conditions. To a smaller extent, sea surface temperature (SST) affects the production of SSA by reducing the kinematic viscosity and surface tension of seawater with increased temperature (Lewis & Schwartz, 2004), which may lead to an increase in the rising speed of bubbles and entrainment efficiency (Forestieri et al., 2018; Jaeglé et al., 2011; Liu et al., 2021; Saliba et al., 2019). However, other studies report a decrease of SSA concentrations with SST (Zábori et al., 2012) or, depending on particle size, both positive and negative relationships (Mårtensson et al., 2003). Other parameters of SSA production are also not yet well researched, but include salinity (Mårtensson et al., 2003) and concentration of surface active materials, which are substances that modify the tension at interfaces (Lewis & Schwartz, 2004; Modini et al., 2013; O'Dowd et al., 2004). Salinity affects surface tension and water density, as well as the mass of sea salt per emitted droplet. It's described by a dimensionless number based on conductivity and lies typically around 35, but varies between 33 and 37 (Lewis & Schwartz, 2004). So far, salinity is not expected to affect SSA production on a large scale due to the relatively constant salinity throughout the global seas, however it may be a more important factor for SSA production on a regional scale (Grythe et al., 2014). Surface active materials are thought to affect water kinematic viscosity and surface tension, leading to altered bubble stabilities and lifetimes (Forestieri et al., 2018). The influence of surface active materials is not yet well understood, but expected to affect mostly sub-micron particles (O'Dowd et al., 2004).

This thesis aims to contribute to this topic of research by investigating parameters affecting the emission of SSA using data acquired during the Atmospheric Emissions and Reactions Observed from Megacities to Marine Areas (AEROMMA) campaign in the summer of 2023, described in detail in Section 3.1. The campaign utilized the NASA DC-8 research aircraft with more than 20 instruments onboard, which were operated during 27 research flights. The data of interest was gathered during four of these flights, which were conducted mostly within the marine boundary layer near the coast of California.

The research questions that were investigated are the following:

- How do wind speed and SST impact the SSA number concentration?
- How does the particle number size distribution vary with wind speed?
- What were the non-SSA contributions to the measured aerosol?

This thesis aims to answer these research questions by presenting the analysis of data gathered by the Cloud and Aerosol Spectrometer (CAS), which measures particle number size distribution between 0.5 and 50 μm in diameter. The sea surface temperature was reported by the Scanning High-resolution Interferometer Sounder (S-HIS). Data on aerosol composition from the Particle Analysis by Laser Mass Spectrometry (PALMS) instrument in the ambient diameter range of 0.5–4 μm was also utilized. Several other instruments provided supporting data, as specified in Section 3.3.

2. Theoretical Background

This chapter provides the background necessary to understand the results presented later in this thesis. Furthermore, it gives the context which will be referred to in the discussion of these results.

2.1. Aerosol Particle Size

Aerosols consisting of particles and ambient air are commonly referred to as atmospheric aerosols and due to their variety of sources span a wide range of properties (Hinds, 1999). Their particle size ranges from a few nanometers (formed from the gas phase) to tens of micrometers (eroded by wind friction) in diameter. For liquid particles, which are almost always spherical, the particle diameter D_p is rather easily definable, however this is more difficult for solid particles which can take on any shape (Hinds, 1999).

In order to make description and comparisons possible for non-spherical particles, equivalent diameters are used: Particles with a certain equivalent diameter share a physical property with a spherical particle of that diameter. This property could for example be volume, aerodynamic behavior or optical behavior. In a first approximation, the true shape can often be neglected if an appropriate equivalent diameter is used. However, this approximation doesn't hold for particles with extreme shapes, such as fibers (Hinds, 1999).

Particle size is one of the most important parameters needed in order to describe the behavior and properties of an aerosol, and can mathematically be represented as shown in Seinfeld & Pandis (1998). An aerosol number distribution $n_N(d_p)$ assigns each infinitesimal size interval $d_p + \mathrm{d}d_p$ the total number of particles of that size per unit volume. Integrating the distribution over the size range returns the total number of particles per unit volume, the number concentration *N*. Because aerosol particle sizes span several orders of magnitude, number concentration is commonly expressed in terms of $\ln d_p$, which is a shorthand for $\ln(d_p/1\mu\mathrm{m})$ in order to work around the technicality that it's not possible to take the logarithm of a dimensional quantity. This yields the following expression for the number concentration *N*:

$$N = \int_{-\infty}^{\infty} n_N(\ln d_p)\mathrm{d}\ln d_p \qquad (1)$$

This can be rearranged to express the number size distribution

$$n_N(\ln d_p) = \frac{dN}{\mathrm{d}\ln d_p}$$

(2)

Depending on the property that is being investigated, the number size distribution might not be the most suitable representation of a sample. Instead, the surface, volume or mass distribution, which describe the surface area, volume and mass of our aerosol particles per unit volume might be needed. By assuming spherical particles (using the appropriate equivalent diameter), the surface area of one aerosol particle can be calculated as $\pi {d_p}^2$. The number concentration and distribution are then multiplied by this factor, which results in the surface concentration and distribution. Analogously, the volume concentration can be calculated by multiplying with the factor $\frac{\pi}{6}{d_p}^3$. Note that the mass concentration/distribution is simply the volume concentration/distribution multiplied with the density of the aerosol particles. Common units are 1/cm^3, µm^2/cm^3 and µm^3/cm^3 for number, surface and volume distribution and concentration, respectively (Seinfeld & Pandis, 1998).

There are several statistical parameters used to describe size distributions, such as the *mean* diameter, which is the arithmetic average of the diameters in a distribution. The *median* diameter is defined as the diameter that separates the larger half of particles from the smaller half of the particles. The *mode* refers to a diameter for which the size distribution exhibits a maximum (Boucher, 2015).

The size distribution of an atmospheric aerosol commonly exhibits up to 5 modes. The smallest mode is called *nucleation mode* and consists of particles formed directly from the gas phase. These particles can grow, resulting in the *Aitken mode*. Nucleation mode and Aitken mode particles range between few nanometers to 100 nm. The *accumulation mode* consists of particles with diameters from 0.1 to 1 µm. Primary aerosols contribute partly to the accumulation mode, but mostly to the largest mode, the *coarse mode*, for which d_p > 1 µm. Some sources define an additional super-coarse mode. (Boucher, 2015). The size ranges listed for the different modes are approximate and also differ depending on the literature source. In ambient conditions, the modes generally aren't distinguishable all at once. Instead, the representation has to be adapted to be able to make out all features: The nucleation and Aitken mode usually dominate the number size distribution, the accumulation mode is most visible in the surface size distribution and the coarse mode appears most clearly in the volume and mass size distribution (Boucher, 2015).

2.2. Aerosol Optical Properties

Aerosol particles interact with radiation in two ways: They scatter and they absorb solar radiation. Particles that mainly absorb visible light appear dark, such as smoke particles. Particles that mostly scatter can appear either light or dark, depending on how much the radiation is scattered (Hinds, 1999).

Depending on the size of the particle, scattering can be described by three different regimes. We quantify particle size within the ratio $\alpha = \pi d_p/\lambda$, where d_p is the particle diameter and λ refers to the wavelength of the radiation (Hinds, 1999).

- Rayleigh scattering occurs for $\alpha << 1$, which describes the relatively uniform scattering in all directions of a particle.
- Mie scattering describes the scattering process for $\alpha \sim 1$ and is much more complicated than the Rayleigh theory. In this size range, particles scatter mainly forward.
- In the limit of $\alpha >> 1$, the Mie scattering morphs into the geometric scattering regime, which describes scattering processes by ray optics (Hinds, 1999; Seinfeld & Pandis, 1998).

The fact that aerosol scattering behavior is dependent on particle size can be used to gather information on it, provided we have some additional information: The wavelength of the incident light and the so-called *refractive index m* have to be known or approximated. The refractive index describes the ratio of the velocity of light in a vacuum and the velocity of light in the material of which the particle is composed, $m = c/v_P$ (Hinds, 1999). Based on this information, the optical equivalent diameter of a spherical particle can be determined (Baumgardner et al., 2001).

2.3. Global Aerosol Burden and Effects

In order to quantify the effects of aerosols on weather, climate and human health, the global distribution and composition of aerosols need to be known. This chapter aims to summarize the mechanisms of aerosol emission and removal, relying mostly on Lohmann et al. (2016).

2.3.1. Sources and Removal

Local concentrations and composition of aerosol particles depend strongly on the nearest sources of aerosols. By mass, the two most abundant aerosol species are sea salt, with an estimated 7925 Tg emitted per year and desert dust with approximately 1678 Tg/year as of the year 2000 (Dentener et al., 2006). Estimations of aerosol production flux of most species vary considerably, but generally the literature agrees at least on the order of magnitude (Boucher,

2015). Since sea salt and desert dust are produced in distinctly different geographical regions, their global distribution differs accordingly: Sea salt is produced anywhere above the ocean surface, but predominantly in the west wind zone (the so-called ‘roaring forties’) and along the storm tracks across the northern Pacific and Atlantic Ocean. Desert dust on the other hand is emitted by wind erosion in arid regions with little vegetation, most importantly the Sahara and Gobi Desert. Anthropogenic emissions tend to be lower in mass, with industrial dust and biomass burning aerosols being the most important contributions, focused in areas of high human activity (Lohmann et al., 2016).

Aerosol removal happens through a process referred to as either scavenging or deposition, which are described in Lohmann et al. (2016). The terms scavenging and deposition are used synonymously. One distinguishes between wet and dry removal processes:

- *Dry deposition* is the sinking and settling of aerosol particles onto the planetary surface due to gravity. This effect is strongest for large, spherical particles and thus it’s the main sink for coarse-mode aerosol particles. Smaller particles are more affected by their Brownian motion, which leads to a decreased settling velocity (Lohmann et al., 2016).
- *Wet deposition* is further divided into impaction and nucleation scavenging. The former describes the process in which a hydrometeor collects aerosol particles, which can occur in the process of precipitation or within clouds. The latter describes the process of aerosol particles acting as CCN or INPs, at which water vapor can condense or deposit, leading to the formation of a hydrometeor. Wet deposition is the primary removal mechanism for nucleation- and accumulation-mode particles (Lohmann et al., 2016).

The lifetime of aerosol particles, i.e. the mean time they spend in the atmosphere, is then mainly dependent on its size and shape, location in the atmosphere and the humidity of its surroundings. This explains why sea salt contributes less to the aerosol burden than dust, even though more sea salt is emitted into the atmosphere: Sea salt is emitted at the ocean surface and usually stays very close to the surface, thus falling back down rather quickly. Furthermore, it’s produced in a humid environment, where wet deposition is strong. In contrast, desert dust is often associated with storms, which can transport the particles high into the atmosphere. Additionally, the dry air in desert regions and high altitudes doesn’t favor wet deposition, which results in a longer lifetime. This leads to a lifetime of approximately 0.5 days for sea salt and 4 days for dust and explains why sea salt is rarely found above continents, but desert dust can be transported from North Africa all the way to Central Europe and America (Lohmann et al., 2016).

2.3.2. Distribution

Earth's atmosphere is separated into five layers: Troposphere, stratosphere, mesosphere, thermosphere and exosphere. The boundaries between the layers depend on latitude, but in the midlatitudes are typically at around 10–15, 45–55, 80–90 and >100 km altitude. Of these, the troposphere contains about 80% of the mass of the atmosphere and is characterized by turbulence and mixing, as well as decreasing temperature with height (Seinfeld & Pandis, 1998). The troposphere is further divided into the planetary boundary layer (PBL), the lowest 1-2 kilometer of the atmosphere, and the free troposphere above it. The two layers are separated by a capping inversion, i.e. a stable layer, which constrains turbulence, pollutants and moisture to the PBL. It also shields the free troposphere from the surface friction, which strongly influences the PBL (Stull, 2006). The height of the PBL can be determined by examining the vertical profile of potential temperature θ, which is the temperature of an air parcel brought adiabatically to standard pressure (Seinfeld & Pandis, 1998). The turbulence within the PBL results in a near constant potential temperature within the PBL and a sharp increase in potential temperature at the boundary (Stull, 2006). Due to the pronounced differences in continental surface temperature over the course of a day, the PBL over land exhibits a diurnal cycle. Above the ocean, this variation is usually negligible due to the large heat capacity of water. Instead, the PBL height over the ocean is governed by large-scale processes of vertical motion as well as advection (Stull, 1988).

Since most aerosol is emitted at the surface the highest concentrations of SSA occur close to the surface. SSA particles with diameters smaller than 2 µm at 80% RH are estimated to be distributed nearly uniformly throughout the marine boundary layer, however this is not true for SSA particles larger than that, which are affected more strongly by gravity (Lewis & Schwartz, 2004). Shinozuka et al. (2004) found a wind speed dependent decrease in sea salt number concentration with sampling altitudes between 0 and 1000 m. The decrease was most pronounced for small surface wind speeds and coarse particles.

Transport and mixing of aerosol make the interpretation of aerosol measurements complex. Gases that are emitted alongside aerosol may give insight into the source of the aerosol measured: Dimethyl Sulfide (DMS) for example is emitted by marine microorganisms, has a lifetime of only about half a day and thus indicates a recent marine influence on an airmass. In the marine boundary layer (MBL), the DMS mixing ratio averages between 80 and 110 ppt, but can increase to up to 1 ppb locally (Seinfeld & Pandis, 1998). Carbon monoxide (CO) on the other hand is emitted whenever incomplete combustion of biomass occurs, such as in industry or during wildfires, and is thus a tracer for continental air. There's a natural background of CO which varies regionally and seasonally within a range of ca. 40 to 200 ppb. With a lifetime of

1-3 months, the elevation of CO values above the background is a suitable tracer to identify continental influences (Seinfeld & Pandis, 1998). To investigate more recent continental influences, sulfur dioxide (SO_2) may be useful, the two main sources of which are anthropogenic activity and volcanic eruptions. Its lifetime is about 2 days in the PBL. In clean MBL air, normal SO_2 values range between 20 to 50 ppt, in continental background air they can be as high as 1 ppb (Seinfeld & Pandis, 1998).

2.4. Sea Spray Aerosol

2.4.1. Production Mechanisms

There are two pathways via which marine aerosols can form: Gases emitted by the ocean can form secondary marine aerosol particles and particle production at the ocean surface leads to emission of primary aerosol particles consisting of saltwater droplets. This thesis focuses on the latter, which is often referred to as sea salt aerosol. However, since these droplets can also contain biological material such as algae or bacteria and pollution like microplastics, the label 'sea spray aerosol' is more fitting (Boucher, 2015). In the following, the abbreviation SSA refers to sea spray aerosol.

There are three main types of SSA particles: Spume drops, film droplets and jet droplets. The production mechanisms of all three are associated with wave breaking, as illustrated in Figure 2.1 and described in de Leeuw et al. (2014) and Veron (2015):

- At wind speeds above 7–11 m/s (de Leeuw et al., 2014; Veron, 2015), so-called *spume drops* are torn off of wave crests just before the wave breaks. These drops are typically very large, from 40 µm to several millimeters in diameter and thus tend to stay close to the surface and have a short lifetime on the order of seconds to minutes in the atmosphere (de Leeuw et al., 2011).
- Once the wave crashes, air bubbles are entrained into the water which later rise back up to the surface, where they form clouds of bubbles called a *whitecap* (de Leeuw et al., 2011). The *whitecap fraction* W is the fraction of the ocean surface covered in whitecaps and is used a proxy for the particle production flux in SSA source functions (de Leeuw et al., 2014). At the surface, the bubbles burst and give rise to two more types of SSA:
    - *Film droplets* are emitted as the bubble breaks and its film cap fragments into particles between 0.02 and 4 µm (Veron, 2015).
    - After the bubble has burst, it leaves behind a cavity in the ocean surface which is filled by the surrounding water, producing one or several *jet droplets*, with a

diameter of about 5–15% of the diameter of the parent bubble (Lewis & Schwartz, 2004), or 2–100 µm (de Leeuw et al., 2011; Veron, 2015).

While one bubble can produce several hundreds of film droplets, it typically produces a maximum of 6 jet droplets, and the number of jet droplets produces decreases with increasing bubble size (Lewis & Schwartz, 2004; Veron, 2015). Consequently, most SSA particles in the atmosphere are film droplets (Lewis & Schwartz, 2004).

In addition to wave breaking, bubbles may be entrained by falling rain, which may thus also be a source of jet and film droplets. However, this mechanism has not yet been researched (Veron, 2015). Other production mechanism of droplets than the ones listed above may exist, but are believed to be less significant. S*plash drops* are produced after a wave breaks and the water impacts on the ocean surface, which emits drops. Due to their size, they likely fall back to the surface quickly, as spume drops do. Furthermore, splash drops are emitted in the lee of the wave crest, which shelters them from wind and makes it unlikely for them to be transported upwards (Veron, 2015).

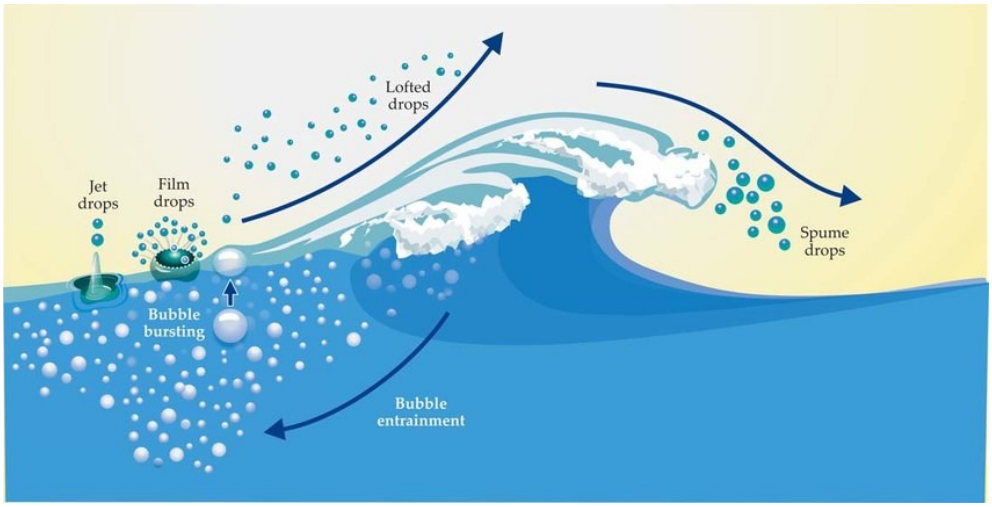

Figure 2.1: Illustration of the production mechanism of SSA. Reprinted from Richter & Veron (2016)

The diameters given in the enumeration above refer to the diameters at a relative humidity of 80%. This is the best measure for jet droplets, which may stay suspended for several minutes to hours, get transported into less humid air and reduce in size due to evaporation (Veron, 2015). This diameter can also be used for film droplets, which may stay suspended for several days. However depending on the humidity of their environment, it may be more fitting to assume full evaporation and use the volume equivalent diameter of the dry particle (Veron, 2015). It is estimated that full efflorescence, i.e. a liquid salt water droplet evaporating and leaving a dry salt particle, only occurs at a relative humidity below 50% (Tang et al., 1997). For

spume drops, which fall back down in a matter of seconds after emission and thus have little time to change size (Veron, 2015), the diameter at formation of the droplet, i.e. immediately after its emission is the most suitable descriptor.

Veron (2015) presents a 'rule of thumb' in order to compare the three diameters,

$$d_{p,0} \sim 2d_{p,80} \sim 4d_{p,d} \quad (3)$$

where $d_{p,0}$ refers to the radius at emission, $d_{p,80}$ to the radius at 80% relative humidity and $d_{p,d}$ to the dry radius.

The expected size distribution of SSA is a result of the three main production mechanisms listed above. The peaks are believed to be centered at $d_{p,80} \sim 100$ µm for spume drops, $d_{p,80} \sim 10$ µm for jet droplets and $d_{p,80} \sim 0.2-1$ µm for film droplets (Veron, 2015). SSA concentrations in the marine boundary layer usually range between 5 and 30 #/cm^3 (Seinfeld & Pandis, 1998)

2.4.2. Properties

Aerosol particles emitted at the ocean surface are of droplets of seawater, which consists primarily of water and sea salt, i.e. dissolved ionic compounds. The most abundant components of sea salt are Cl^-, Na^+, Mg^{2+}, SO_4^{2-}, Ca^{2+}, K^+ and HCO_3^- (Lewis & Schwartz, 2004). The concentration of these solutes can quantified by the salinity, which is a measure of conductivity and is roughly equal to the mass ratio of dissolved material in grams per kilogram of seawater (Lewis & Schwartz, 2004).

Since SSA particles are emitted as liquid droplets, they can be well described as spherical. This approximation holds as long as the ambient RH stays above the efflorescence RH of ~50% (Lewis & Schwartz, 2004; Tang et al., 1997). Furthermore, above this threshold, the refractive index of an SSA particle with a fixed amount of dissolved sea salt depends only weakly on RH (Lewis & Schwartz, 2004) and any variation will be neglected in the present work. At the commonly used 80% RH and a wavelength of 650 nm, the refractive index has recently been estimated to be around 1.38 (Fan et al., 2025).

3. Methods

3.1. The AEROMMA Campaign

As described briefly in the Introduction, the Atmospheric Emissions and Reactions Observed from Megacities to Marine Areas (AEROMMA) study was an airborne research project conducted between June and August of 2023, led by NOAA's Chemical Sciences Laboratory. It consisted of 27 flights onboard the NASA DC-8 research aircraft. The University of Vienna contributed to the project by bringing the Cloud, Aerosol and Precipitation Spectrometer (CAPS) and the Precipitation Imaging Probe (PIP) on board. The instruments are further described in Section 3.2. The CAPS and its position on the wingtip of the DC-8 is depicted in Figure 3.1.

Figure 3.1: Left: Map of the western coast of California depicting the marine flights of the AEROMMA project. Top: The AEROMMA logo (*AEROMMA*, n.d.). Top right: The NASA DC-8 research aircraft (*AEROMMA Platform: NASA DC-8*, n.d.). Bottom right: The CAPS instrument. The black square indicates the position of the instruments on the plane.

During this project, three environments were investigated: The urban atmosphere, the urban-marine interface and the marine atmosphere. This thesis will focus solely on the marine part of the project, which consists of four flights, in the following referred to as 'marine flights'. They were conducted on the 16th, 19th, 21st and 23rd of June 2023 and were performed out of

Palmdale, CA, also marked on the map in Figure 3.1. To research the pristine marine atmosphere, the measurements were limited as far as possible to regions with moderate anthropogenic impacts, stable meteorology, well-defined boundary layers and varying clouds fields (*AEROMMA Goals*, n.d.). While the project investigates a broad range of topics within marine atmospheric physics and chemistry, this thesis focuses on large accumulation and coarse mode aerosol measurements.

3.2. Instrumentation: The UNIVIE-CAPS

This thesis presents data acquired by the University of Vienna's second-generation Cloud, Aerosol and Precipitation Spectrometer (UNIVIE-CAPS), the wing-mounted probe depicted in Figure 3.2. In this chapter, its working principle and instrument-specific operating procedures will be discussed.

3.2.1. Working Principle

The CAPS consists of several sensors: The Cloud and Aerosol Spectrometer (CAS), the Cloud Imaging Probe (CIP), the Liquid Water Content Detector (LWCD), as well as sensors that quantify air speed, relative humidity and temperature. The two main sensors CAS and CIP are indicated in red and green respectively in Figure 3.2. In the present work, only data acquired by the CAS is analyzed, therefore the CIP will not be described.

The CAPS is manufactured by DMT (Droplet Measurement Technologies Inc., Longmont, CO, USA) and was first presented and described in Baumgardner et al. (2001).

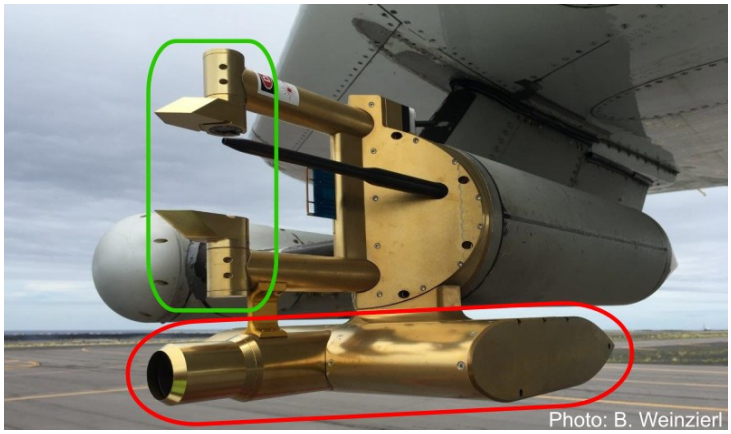

Figure 3.2: The UNIVIE-CAPS. Marked in red: The CAS. Marked in green: The CIP arms.

The CAS is an optical particle spectrometer, which detects and sizes particles between 0.5 and 50 µm (Dollner et al., 2024). Its key element is a laser beam with a wavelength of 658 nm, which is scattered by particles passing through it. Figure 3.3 depicts the stream of air from top to bottom, and the laser traversing the stream from right to left. The light scattered by an

aerosol particle is detected either by the forward scattering detector in an annular range of 4° to 12° or by the two backward detectors in an annular range of 168° to 176° (Glen & Brooks, 2013). The forward detector is complimented by an additional detector with an optical mask, which limits the measurement to particles in the depth of field of the instrument. The sample volume is defined by a pinhole aperture (Baumgardner et al., 2001).

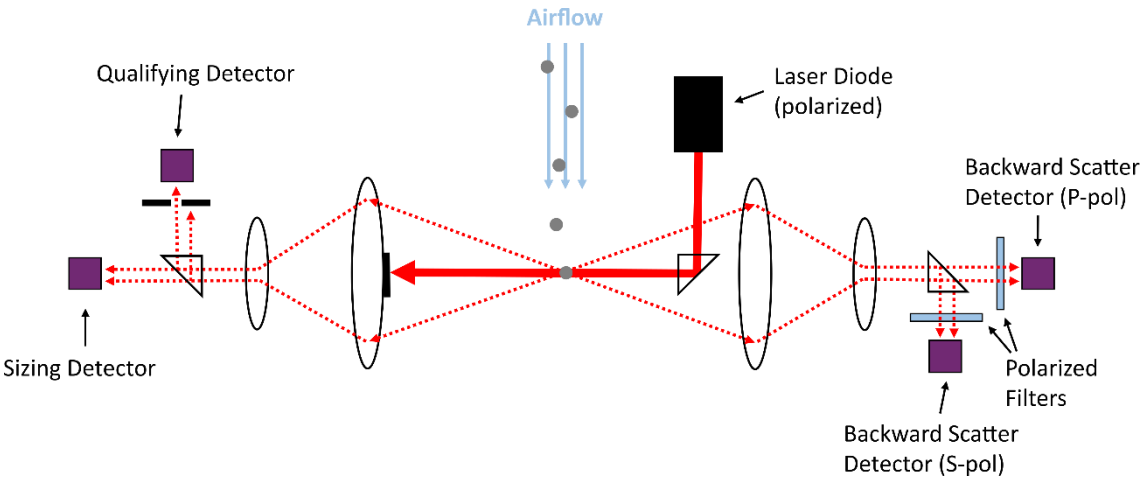

Figure 3.3: Schematic of the CAS. Adapted from Droplet Measurement Technologies, Inc., (2009).

The data acquired by the UNIVIE-CAPS is initially available within two data products: A timeseries contains housekeeping data (such as laser temperature and voltage), volume and number concentrations and binned size distribution. Additionally, particle-by-particle (PbP) data contains single-particle information, including the forward scattering signal amplitude, which can be converted to a scattering cross section using the calibration procedure described in the section below. This yields the optical equivalent particle size (Dollner, 2022).

3.2.2. CAS Calibration

In order to ensure reproducibility, the CAS is calibrated regularly in between research flights, ideally the day before or on the day of each flight. The procedure is described in detail in Dollner (2022) and Dollner et al. (2024). The calibration aims to determine the relationship between scattering signal amplitude and the scattering cross section, which will be discussed in more detail later in this section. Figure 3.4 depicts the setup for a CAS calibration, which can be performed both in the field and in the lab. The CAS sampling tube is connected to form a closed loop of tubing, in which the air is circulated by a centrifugal fan and filtered by a HEPA filter. Calibration particles are mobilized and injected into the airstream just in front of the CAS inlet, in order to reduce sedimentational losses to a minimum (Dollner et al., 2024).

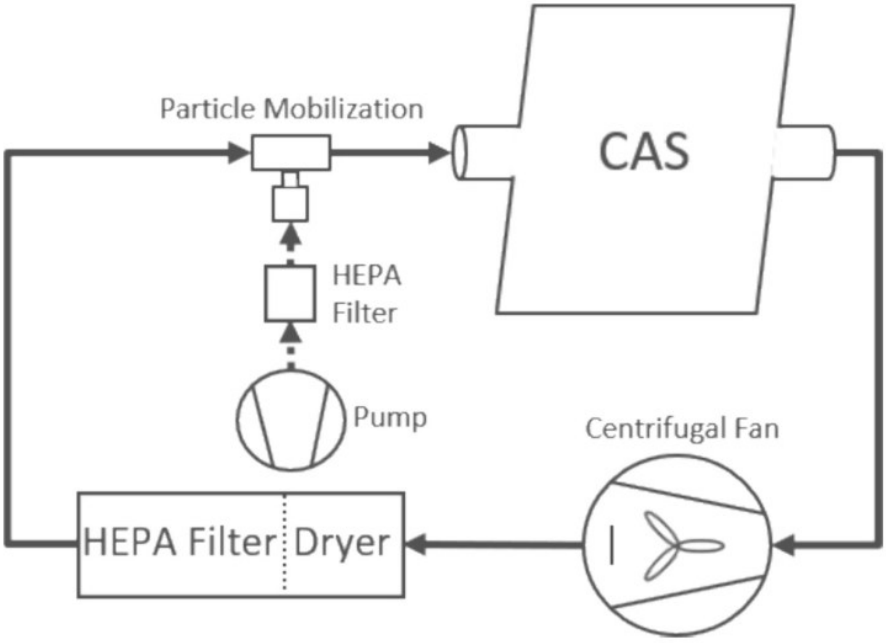

Figure 3.4: The calibration setup of the CAS. Reprinted from (Dollner et al., 2024)

The calibration particles span the entire CAS sizing range from 0.5 to 50 µm and consist of polystyrene latex spheres (PSL) and glass (soda-lime or borosilicate) of known size and refractive index as certified by the United States National Institute of Standards and Technology (NIST). Particles of one size are injected into the airstream and the CAS produces a distribution of scattering signal amplitudes, which is used to calculate the scattering cross-section. Doing so for several calibration standards results in the instrument-specific relationship between the two quantities, which is linear for the CAS. For each calibration, the linear relationship is fitted and the calibration output are the fit coefficients, which allows a conversion of any measured scattering signal amplitude into a scattering cross-section (Dollner et al., 2024). The optically equivalent particle size can then be determined using Mie Theory for the particle's refractive index. (Dollner et al., 2024).

3.3. Other Instruments

While results presented in this thesis are based mostly on CAPS data, several data products provided by other research teams have been utilized in order to analyze it. In the following, these instruments are introduced briefly in alphabetical order. A list of all deployed instruments can be found at *AEROMMA Platform: NASA DC-8 Payload* (n.d.-b).

Diode Laser Hygrometer (DLH)

The relative humidity with respect to water is a crucial variable in the Cloud Indicator (see Section 3.5) and used to estimate boundary layer height in this thesis. It is reported by a Diode Laser Hygrometer (DLH), together with the relative humidity with respect to ice and the water vapor mixing ratio. This instrument was developed in 2002 for use on the NASA DC-8 and utilizes wavelength modulated differential absorption spectroscopy, operating in the near-infrared spectral region (Diskin et al., 2002). The data used in this thesis is reported with a resolution of 20 Hz and an uncertainty of 15%.

Los Gatos Research CO/N2O Analyzer (LGR)

The Los Gatos Research CO/N2O Analyzer uses off-axis integrated cavity output spectroscopy (ICOS) technology to determine gas mixing ratios of CO, N_2O and H_2O. Its measurement principle is based on cavity-ringdown spectroscopy, i.e. the absorption of laser light by gas molecules (Springston et al., 2025). The instrument team reports the data with a temporal resolution of 1 Hz and the CO measurement has an uncertainty of ± (0.2 ppb + 2%).

Meteorological Measurement System (MMS)

The Meteorological Measurement System (MMS) is an instrument originally described in a publication from 1990, which details the usage on NASA's high-altitude research aircraft ER-2 (Scott et al., 1990). The instrument provides in situ measurements of free-stream pressure and temperature with an uncertainty of ±0.3 hPa and ±0.3 K respectively and the wind vector with an uncertainty of ± 1 m/s of each coordinate. The temporal resolution is 20 Hz. It has since been installed on several types of research aircraft, including the NASA DC-8, and has been deployed during various measurement campaigns, among them AEROMMA 2023. The analyses presented in this thesis utilize the reported wind vector as well as potential temperature and true airspeed, both of which are secondary data products provided by MMS. It also supplies flight altitude in WGS84 coordinates. For more information on this instrument, see NASA Airborne Science Program (n.d.)

Particle Analysis by Laser Mass Spectrometry (PALMS)

The Particle Analysis by Laser Mass Spectrometry (PALMS) instrument is a single particle mass spectrometer which provides information about the chemical composition of aerosol particles (Murphy et al., 2006). It determines aerosol composition by evaporating individual particles and ionizing their components using a laser pulse. The produced ions are then analyzed using a time-of-flight mass spectrometer. The aerosol composition is quantified by attributing each particle to one of nine particle classes based on the dominant spectral

signatures: Sulfate–organic–nitrate mixtures, biomass burning, sea salt, mineral dust, elemental carbon, alkali salts, meteoric material, heavy fuel oil combustion, and unclassified particles. While PALMS does have the capability to analyze internally mixed particles, for the AEROMMA campaign any particle containing sea salt was classified as sea salt, including SSA particles containing organics or other material. Aerodynamic particle size is determined by measuring the single-particle flight time between two detection lasers before ionization. The flight time is then estimated based on laboratory calibrations using polystyrene latex sphere size standards from Duke Scientific (Froyd et al., 2019). The aerodynamic particle size is then converted to volume-equivalent particle size using particle densities and dynamic shape factors (Froyd et al., 2019).

Scanning High-resolution Interferometer Sounder (S-HIS)

The sea surface temperature was measured and reported by a Scanning High-resolution Interferometer Sounder (S-HIS). It measures thermal radiation emitted by the planetary surface with a spectral resolution of 3.3–18 µm and an angular field of view of 0.1 radians, which corresponds to approximately 20 m at 200 m flight altitude (Tobin et al., 2006). This analysis uses the reported values for sea surface temperature, which are given at a temporal resolution of 1 Hz.

3.4. HYSPLIT

NOOA's Air Resources Laboratory's Hybrid Single-Particle Lagrangian Integrated Trajectory model (HYSPLIT) (Draxler, 1999; Draxler & Hess, 1997, 1998; Stein et al., 2015) is a model for computing air parcel trajectories and furthermore transport, dispersion, chemical transformation and deposition simulations. It combines a Lagrangian and Eulerian approach: It uses a moving frame of reference (Langrangian) to compute advection and diffusion in order to track air parcels and a fixed grid (Eulerian) to calculate air pollutant concentrations (Stein et al., 2015). In this thesis, matrix backward trajectories of air parcels were calculated using the online READY web-version of HYSPLIT (Rolph et al., 2017; Stein et al., 2015), reaching 120 hours into the past. The meteorological dataset used was the global forecast system (GFS, global, 0.25° resolution). For each date, a grid of endpoints was defined that matches the regions in which measurements were recorded. The grid has a spatial resolution of 1°x1° for each simulation. In the table below, the south-western and north-eastern points of the grids are given as well as the time at which the backward trajectories ended. Note that flight 20230616 was split up into a northern and a southern region, which will further be explained in Section 5.2.

Table 3.1: For each flight: Coordinates of the corner points of the defined 1°x1° grid for which the HYSPLIT trajectories were calculated and the time of day at which the trajectories end.

	South-Western point	North-Eastern point	Trajectories ending at (UTC)
20230616 (North)	127°W 37°N	125°W 39°N	21:00
20230616 (South)	125°W 24°N	122°W 26°N	00:00 (June 17th)
20230619	122°W 29°N	120°W 35°N	19:00
20230621	131°W 41°N	125°W 43°N	23:00
20230623	125°W 32°N	123°W 35°N	20:00

3.5. Data Selection and Processing

CAPSlib

The raw data acquired by the UNIVIE-CAPS is processed by the CAPSlib algorithm, which was developed by Dollner (2022). The algorithm requires MMS and DLH data in addition to CAPS data and calculates number size distributions, number concentrations and an additional data product (the cloud flag) described below, based on the raw data provided by the instruments. Initially, a quality flag is calculated, which indicates a problem with the measurement if the value is not zero. It distinguishes 4 cases of common problems that might occur: The quality flag returns the value 1 if the sizer high baseline is above the reference value. A value of 2 is given if the forward block temperature drops below 19°C, which impacts the performance of the CAS and leads to noise in the data. The value 4 corresponds to a drop of the laser current below 95 mA, which indicates that the laser is not working optimally and may be overheating. A quality flag of 8 is returned when time errors occur in the raw data. Any data yielding a non-zero quality flag is excluded from further processing.

As described in Section 3.2, the optical equivalent particle diameter is calculating by applying Mie Theory to the scattering cross section derived from the measured signal amplitude. This requires knowledge of the particles refractive index. Since for in-field measurements the refractive indices of individual particles are generally unknown, a fixed refractive index is assumed instead. For the AEROMMA campaign, the data was processed using four refractive indices: 1.31, 1.33, 1.52 and 1.56. Based on the Mie curve for the selected index, each scattering cross section is assigned to a particle size. However, because the Mie curve oscillates, one scattering cross-section can correspond to several particle sizes. This is solved by binning particle sizes into bins large enough to encompass these oscillations. This results in 15 CAS-bins with varying widths. Size ranges given in this thesis always refer to the left

boundary of the smaller bin and the right boundary of the larger bin. Section 3.2 also mentions the presence of backward scatter detectors within the CAS, the data provided by which is currently not being processed. If included in the analysis, it will give information on the shape of the particles, which will allow the determination of geometric particle size by using discrete dipole approximation to compute the scattering cross section functions for different orientations of the non-spherical particles.

To improve the sampling statistics for the larger particles, which are difficult to mobilize, a Monte Carlo method is applied to the data (Metropolis & Ulam, 1949). Random resampling of the measured scattering signal amplitudes and the calculated scattering cross-sections per standard results in a dataset which reflects the variability and uncertainty of the original data. In the current version of the data processing software, this is not fully implemented yet. In the future, this will allow an improved fit and determination of the covariance of the relationship. It will also enable uncertainty propagation to particle size, which is currently not possible (Dollner et al., 2024). The CAPSlib also takes a value for a 'time offset' for each flight, which it uses in the processing to eliminate the time difference between different instruments, caused by their relative position on the airplane. The data analyzed in this thesis is field-quality data (version RA), which means that the time offset has not yet been determined. The time offset for the AEROMMA flights is expected to be in the order of seconds. While this should be considered when comparing CAPS data to data provided by other instruments, it's not expected to significantly affect the results presented in this thesis.

The CAPSlib also calculates the cloud flag, which is a data product based on the cloud indicator algorithm recently developed by Dollner et al. (2024). The cloud indicator differentiates between cloud free periods, aerosol cloud transition regime (ACTR), liquid clouds, mixed phase temperature regime, and cirrus clouds based on temperature, RH, aerosol size distribution and a newly introduced aerosol volume factor. The cloud flag classifies cloud-free periods and ACTR as 'cloud-free' and liquid clouds, mixed phase temperature regime, and cirrus clouds as 'in-cloud'. It also flags measurement periods of 10s and less between 'in-cloud' periods as 'in-cloud' (Dollner et al., 2024).

Determination of the Boundary Layer Height

The analysis was limited to data sampled within the boundary layer. To determine the boundary layer height (BLH), the vertical profiles of potential temperature and relative humidity were analyzed. As described in Section 2.3.2, the potential temperature exhibits a characteristic sharp increase at the BLH and due to this capping inversion, moisture is trapped in the boundary layer. The BLH in this thesis was determined by finding the altitude of the capping

inversion in the potential temperature profile and supported by the relative humidity profile. Because the boundary layer fluctuates regionally, some variation in the BLH is expected over the course of a flight. The BLH per flight was fixed at the lowest altitude exhibiting the sharp increase, rounded to the nearest 10 m.

Calculation of Wind speed

The 3D-wind speed was calculated based on the wind vector (u, v, w) provided by the MMS instrument using the formula

$$ws = \sqrt{u^2 + v^2 + w^2} \quad (4)$$

where u is the west-to-east horizontal wind, v is the south-to-north horizontal wind and v is the vertical wind. Using gaussian error propagation and the uncertainty of ±1 m/s given for each coordinate, we calculate a total uncertainty for the wind speed of ±1 m/s.

Modulation by Sea Salt Fraction

As described previously, the CAS measures particles with diameters between ca. 0.5 and 50 µm, depending on the chosen refractive index. Particles of these sizes will not all be marine in origin, even in a marine environment with all the constraints listed above applied. Section 2.3.1 briefly describes how aerosol transport affects the marine aerosol burden. To ensure that the analysis in this thesis, which aims to answer questions about SSA, takes only particles emitted by the ocean into account, data provided by the PALMS instrument is used.

For the AEROMMA campaign, the PALMS team provided particle-by-particle aerosol compositional data for particles with diameters > 0.1 µm at a RH of < 40%, which is considered dry. In order to convert the particle sizes to ambient RH for this thesis, the growth factor was calculated for each particle using the iterative formula presented in Petters & Kreidenweis (2007):

$$GF = \sqrt[3]{1 + RH \cdot \frac{GF^3 - 1 + \kappa}{e^{4\sigma_{s/a} M_w / (RT\rho_w d_{p,d} \cdot GF)}}}, \quad (5)$$

where ρ_w is the density of water, M_w is the molecular weight of water, $\sigma_{s/a}$ is the surface tension of the solution/air interface, R is the universal gas constant, T is temperature, and $d_{p,d}$ is the diameter of the dry particle (Petters & Kreidenweis, 2007). The parameter κ was introduced by Petters & Kreidenweis (2007) as the hygroscopicity parameter and quantifies

water uptake and CCN activity of aerosol particles. For the present work, the hygroscopicity parameter of NaCl, the primary component of SSA, was used.

The temperature was provided by MMS and the particle size by PALMS. The other variables in the calculations were treated as constants with the following values:

Table 3.2: List of variables needed to calculate the GF and the values used in this thesis.

Variable	Value	Reference
ρ_w	$1000\ kg/m^3$ (at STP conditions)	Linstrom & Mallard (n.d.)
M_w	$18{,}02\ \cdot\ 10^{-3}\ kg/mol$	Linstrom & Mallard (n.d.)
$\sigma_{s/a}$	$0{,}073\ N/m$ (at STP conditions)	Kalová & Mareš (2015)
R	$8{,}3145\ J/(K \cdot mol)$	Tiesinga et al. (2021)
κ	1.12	Petters & Kreidenweis (2007)

The GF was calculated iteratively until the change was smaller than 0.1%.

In order to use PALMS data together with CAS data, the size ranges have to be matched as well as possible. The PALMS team recommends applying an upper diameter limit of 4 µm to their data, since particles larger than that are affected by inertial losses in the inlet. The lower limit is determined as 0.5 µm by the CAS. Thus, only particles between 0.5 and 4 µm are considered when calculating the PALMS fractions. Due to the non-uniform CAS bins, it's not possible to restrict the CAS size range to the exact same values. The closest possible size range was selected, which includes CAS bins 1–6, at a refractive index of 1.33 corresponding to a size range of 0.53–5.10 µm. Note that PALMS and CAPS report different equivalent diameters (volume equivalent and optical equivalent diameters, respectively), which are not necessarily comparable. Section 4.2 will elaborate on this.

The PALMS team also recommends that every time interval for which the fractions are calculated should contain at least 10 particles. In accordance with this, the PALMS number fractions were calculated in 1-minute-intervals. These number fractions are then linearly interpolated to a resolution of 1 second, to match the CAS temporal resolution.

The number concentration reported by the CAS is multiplied by the interpolated PALMS sea salt fraction. Since PALMS assigns any particle containing sea salt to the species sea salt, SSA particles enriched in organics or other materials are also classified as sea salt. Consequently, by modulating the CAS number concentration by the PALMS sea salt fraction we obtain the number concentration of SSA particles.

4. Results

4.1. Data Selection

Not all data sampled during the marine flights is suitable to answer the research questions stated in the Introduction. Since SSA particles are emitted at the ocean surface, any data acquired above land was excluded to ensure a marine environment and only data within the boundary layer was considered. Furthermore, any occurrences of clouds were excluded using the cloud flag described Section 3.5. Consequently all data points flagged as liquid clouds, mixed phase temperature regime, and cirrus clouds as well as periods of 10s and less between them are considered ‘in-cloud’ and excluded from further analysis (Dollner et al., 2024)

Figure 4.1 shows the vertical profiles of potential temperature and relative humidity of the four marine flights. For the three flights 20230616, 20230619 and 20230623 the capping inversion associated with the boundary layer is very apparent. Unfortunately, it was not possible to determine the BLH of flight 202321 with confidence. Note that flight 20230616 took place in two distinct regions, which resulted in two different BLHs.

Determining the BLH as described in Section 3.5 results in the following values:

Table 4.1: Determined minimum boundary layer height for each flight.

Flight	Minimum boundary layer height
20230616	280m
20230619	560m
20230621	undetermined
20230623	1300m

In order to minimize altitude-dependent effects on the SSA concentration and properties, the lowest determined BLH was used as a constraint for all data. Consequently, only data acquired at or below 280 m of flight altitude was considered for all flights. Periods of rapid ascent or descent were additionally excluded from the data.

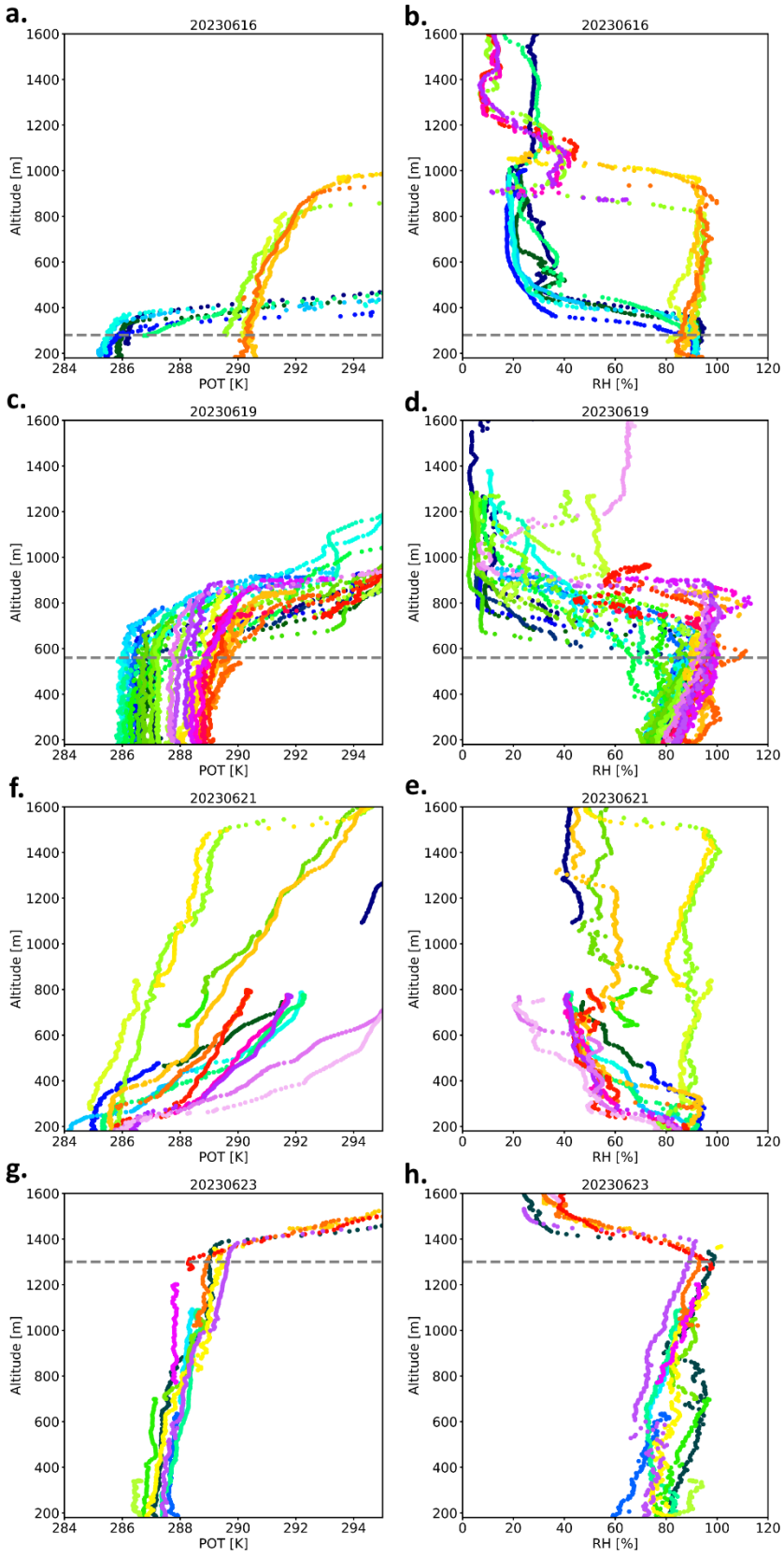

Figure 4.1: Vertical plots of ascents and descents above the ocean surface. The colors differentiate between vertical profiles. The determined BLHs are indicated by dashed horizontal lines. Subplots a, c, e and g show altitude vs. potential temperature. Subplots b, d, f and h show altitude vs. RH.

Applying the criteria described above, we are left with approximately 10 hours and 9 minutes of data. These periods, i.e. horizontal flight segments at or below 280 m above the ocean in non-cloudy areas will be referred to as *periods of interest* and are depicted in Figure 4.2. The image on the left shows the flight tracks of the four marine flights on a map, with the periods of interest in the darker colors. On the right, the four marine flights are plotted as timeseries of altitude, with the periods of interest in color. All data presented in the following refers only to the periods of interest.

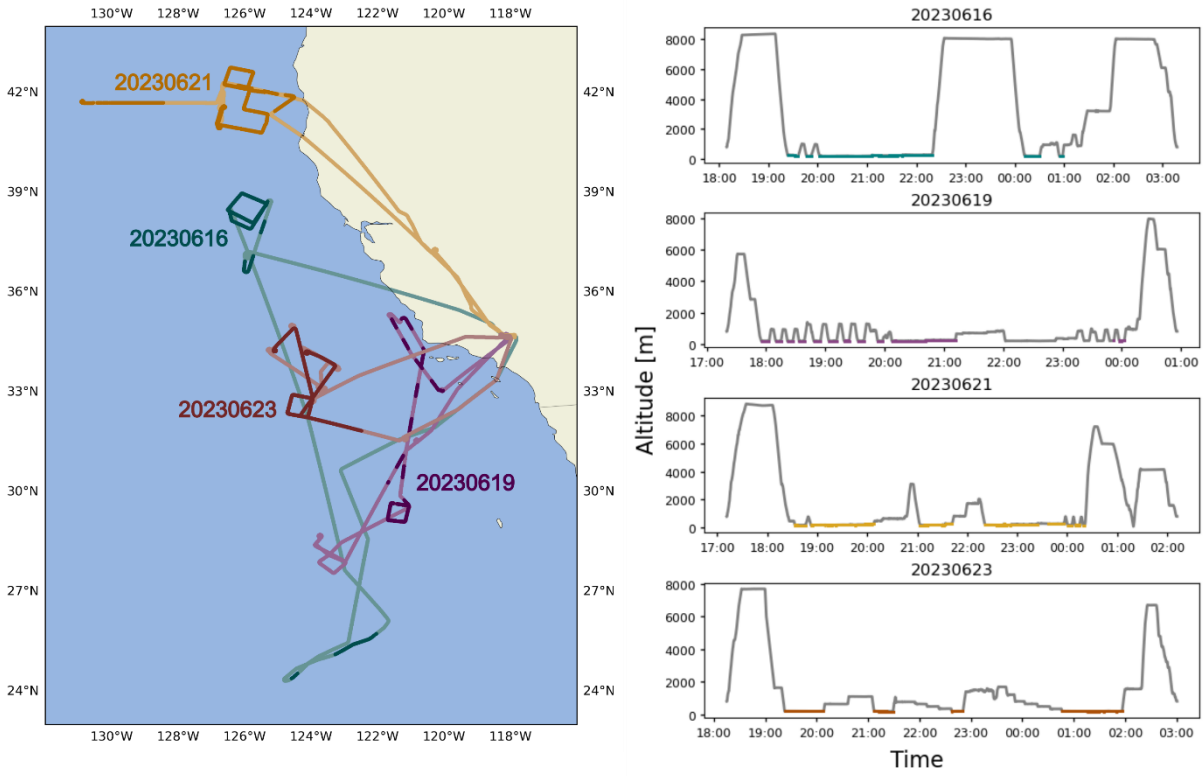

Figure 4.2: Left: Map of flight tracks. The darker colors mark segments fulfilling the constraints. Right: Timeseries of flight altitude. The periods fulfilling the conditions are colored.

The modulation of CAS data described in section 3.5 reduces the amount of valid datapoints to ca. 8 hours and 40 minutes due to some gaps in the PALMS dataset.

4.2. Ambient Conditions and Aerosol Composition

Over the course of the periods of interest, the ambient temperature varied between (272.7 ± 0.3) K and (291.3 ± 0.3) K and the median temperature was (286.7 ± 0.3) K. Note that there was only one datapoint with a temperature < 273.15 K. Given this, we assume any water in the atmosphere to be in a liquid state. The relative humidity, depicted in a timeseries in Figure 4.3, ranged between (49 ± 7)% and (97 ± 14)%, with a median at (83 ± 12)%.

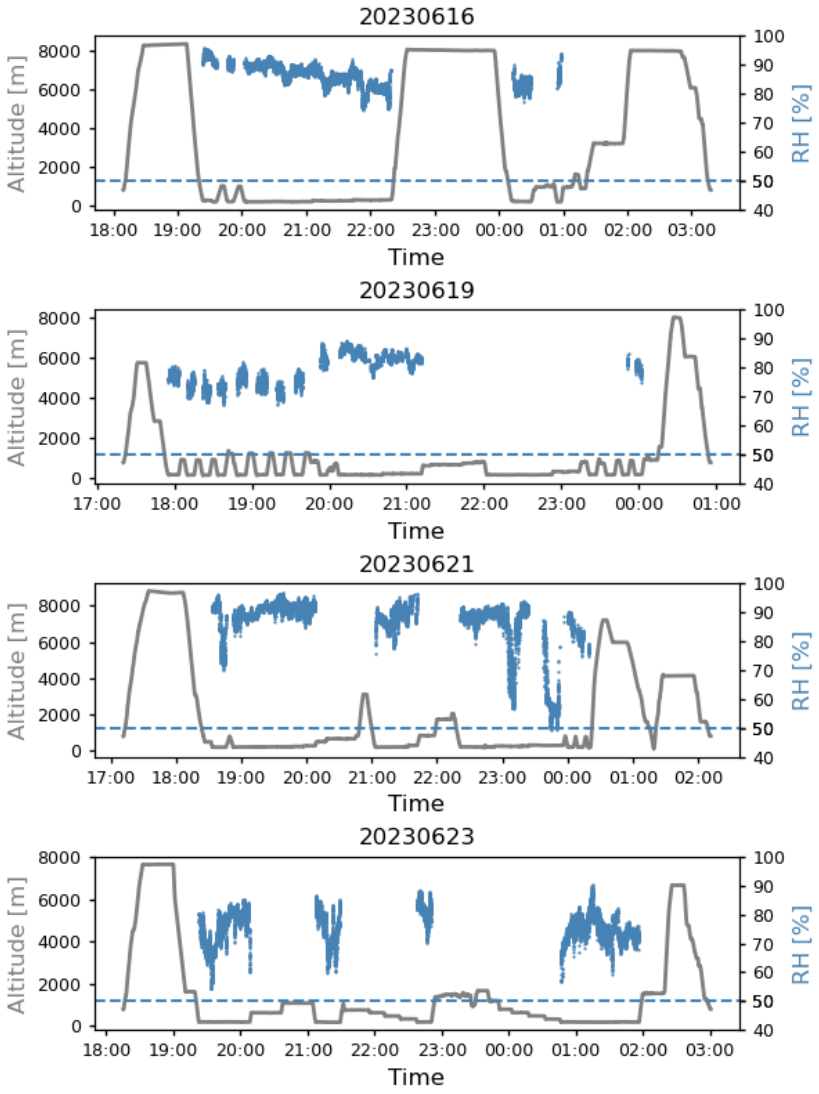

Figure 4.3: Timeseries of flight altitude and relative humidity. The latter is plotted only for the periods of interest. The efflorescence humidity is indicated by the dashed blue line.

As described in Section 2.4.1, efflorescence of SSA particles occurs at a relative humidity below 50%. This threshold is fallen short of in only 5 datapoints during flight 20230621. Consequently, we assume any sea salt in the atmosphere to be fully dissolved in water and thus to be spherical in shape, which means that the optical equivalent diameter reported by the CAS is equal to the geometric diameter. We presume that this is comparable with the PALMS volume-equivalent diameter, which for spherical particles is also equal to the geometric diameter. The particles measured by PALMS are generally not spherical due to the low relative humidity in the instrument, however after applying the growth factor we assume the particles to be liquid again. In these conditions, we approximate the refractive index of SSA particles with the refractive index of water, namely 1.33 (Fan et al., 2025), which is the closest available value to the estimated 1.38 discussed in Section 2.4.2.

The composition of aerosol particles with ambient diameters between 0.5 and 4 µm as measured by the PALMS instrument is depicted in Figure 4.4. It plots volume-equivalent diameter versus the composition as a number fraction per category.

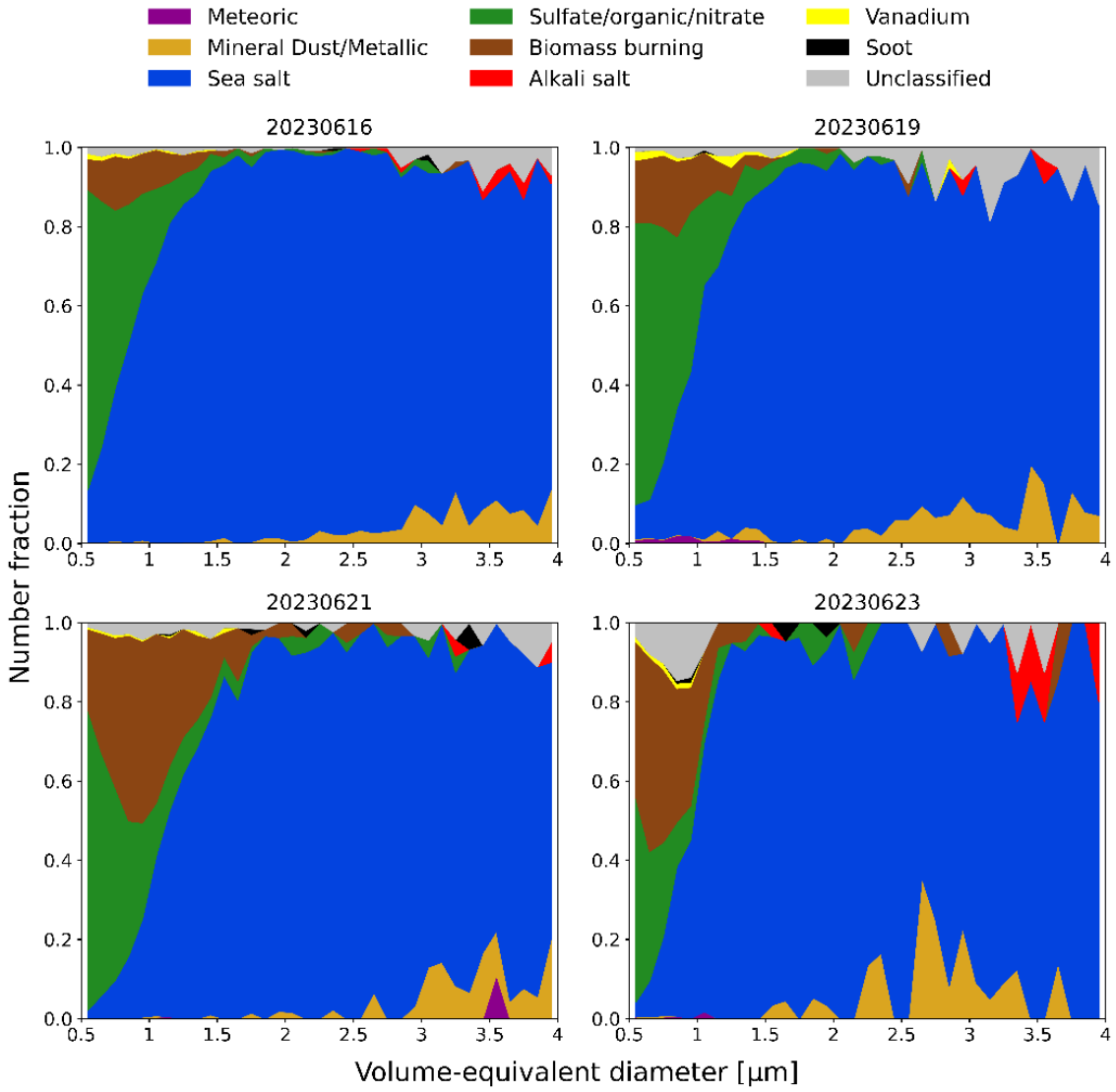

Figure 4.4: Composition of aerosol particles with volume-equivalent diameters between 0.5 and 4 µm at ambient RH.

On all flight days, sea salt is the dominating fraction overall. For diameters smaller than ca. 1 µm, the most abundant species is either sulfate/organic/nitrate with 61%, 63% and 60% for flight 20230616, 20230619 and 20230621 respectively or biomass burning with 42% during flight 20230623. Note that the contribution of biomass burning to the accumulation mode of flight 20230621 was 30%, as listed in Tables A.1–A.4. The average sea salt fraction for partices with diameters of 0.5 to 1 µm is 14%. Of the particles between 1 and 1.5 µm, 72% are sea salt, however the dominating species of the accumulation mode are still influential. For particles

with diameters between 1.5 and 4 µm, sea salt is the most abundant species with 89%. In this size range, no other species makes up more than 4% of the particles measured.

4.3. Number Concentration

The median number concentration of particles between 0.53 and 5.10 µm measured by the CAS instrument was 21.44 cm^{-3}, 5.81 cm^{-3}, 4.76 cm^{-3}, 3.98 cm^{-3} per flight respectively. In the following, this quantity is referred to as the *particle number concentration*. Modulating by the sea salt fraction as described in Section 3.5 results in median number concentrations of 11.11 cm^{-3}, 3.16 cm^{-3}, 0.57 cm^{-3} and 0.87 cm^{-3}, in the following referred to as *SSA number concentration*. In the next two sections the dependence of particle and SSA number concentration on wind speed and sea surface temperature will be presented. All number concentrations are calculated to standard temperature and pressure (STP) conditions, which are 273.15 K and 101.325 kPa.

4.3.1. Dependence on Wind Speed

The wind speed during the marine flights ranged from (1 ± 1) m/s to (31 ± 1) m/s overall. The detailed ranges of wind speed per flight are listed in Table 4.2. Flight 20230616 exhibited the highest wind speeds, exceeding the wind speeds of the other days by more than 10 m/s. The lowest wind speeds were measured during flight 20230623.

Table 4.2: Wind speed during the marine flights.

	Wind speed [m/s], ± 1 m/s		
Flights	**Minimum**	**Median**	**Maximum**
20230616	7	21	31
20230619	5	10	19
20230621	2	10	22
20230623	1	5	10

Figure 4.5 shows a side-by-side comparison of the relationship between particle number concentration vs. wind speed and the SSA number concentration vs. wind speed. The relationship is plotted for each date separately, as indicated by the color code. The wind speed bins have a width of 2 m/s and for each bin the median is indicated by the scatterplot. The amount of datapoints per bin is indicated by filled/empty markers: Bins with less than 60

seconds worth of data are represented by empty markers. The shaded areas correspond the 10th and 90th percentiles.

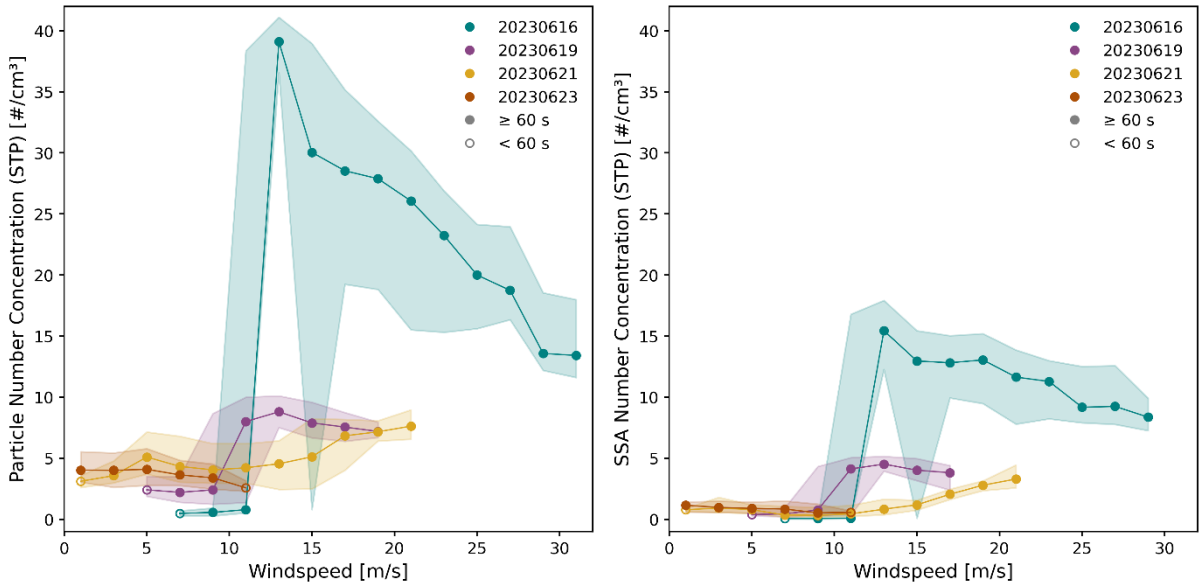

Figure 4.5: Particle number concentration (left) and SSA number concentration (right) of particles between 0.53 and 5.10 µm plotted against wind speed. Wind speed bins are 2 m/s, point mark the median and the shaded areas correspond to the 10th and 90th quantiles. Filled markers indicate that 60 or more datapoints are considered in the respective bin, empty markers indicate that less than 60 datapoints fall into the bin. The solid lines connect the datapoints to guide the eye.

There is a clear difference between the order of magnitude of particle and SSA number concentration. While the particle number concentration has a maximum of 39.10 #/cm^3 in the wind speed bin (12 m/s, 14 m/s], the SSA number concentration peaks at 15.44 #/cm^3 at the same wind speed. Despite these differences in absolute magnitudes, the relationships between number concentration and wind speed are similar for particle and SSA number concentrations. For wind speeds lower than 10 m/s, neither particle nor SSA number concentration show any clear dependence of wind speed. Flight 20230616 exhibits a steep increase from an SSA concentration of 0.09 #/cm^3 at wind speeds between 10 and 12 m/s to 15.44 #/cm^3 in the next bin. A less steep increase occurs during flight 20230619, from 0.77 #/cm^3 at 8–10 m/s to 4.13 #/cm^3 in the next bin. The concentrations of flight 20230616 shows a decrease after this peak and the number concentrations of flight 20230619 level off. Flight 20230621 exhibits a steady increase starting in the bin (12 m/s, 14 m/s] and a maximum SSA concentration of 3.30 #/cm^3 at the highest measured wind speeds between 20 and 22 m/s. During flight 20230623, no wind speeds larger than 10 m/s were measured and there is no apparent correlation between number concentration and wind speed.

4.3.2. Dependence on Sea Surface Temperature

The sea surface temperature over the course of the four research flights exhibited a variation of more than 10 K between 283 K and 295 K. In the median, flight 20230616 was the warmest and flight 20230621 was the coldest, with the other two flights spaced out between them. The spread was about 10 K for three out of four flights: Flight 20230623 is the exception with a spread of only 7 K. More details are listed in Table 4.3.

Table 4.3: Sea surface temperature during the marine flights.

	Sea Surface Temperature [K]			
Flights	**Minimum**	**Median**	**Maximum**	**Spread**
20230616	284	292	294	10
20230619	286	290	295	9
20230621	283	287	292	9
20230623	287	289	294	7

The relationship of particle and SSA number concentration versus wind speed is plotted in Figure 4.6. As in the previous section, the absolute values of number concentration decrease strongly with the modulation by sea salt fraction. However, there is again little difference in the general trends. Flight 20230616 and 20230619 behave similarly in both particle and SSA number concentration. Both quantities are mostly level at a SSA concentration of ca. 15 #/cm^3 between 285 K and 290 K, then decrease sharply to close to zero from 290 K onwards. Flight 20230621 shows a slight increase in number concentrations towards the lowest temperatures, but remains constant otherwise. Flight 20230623 shows no discernible relationship between number concentration and sea surface temperature.

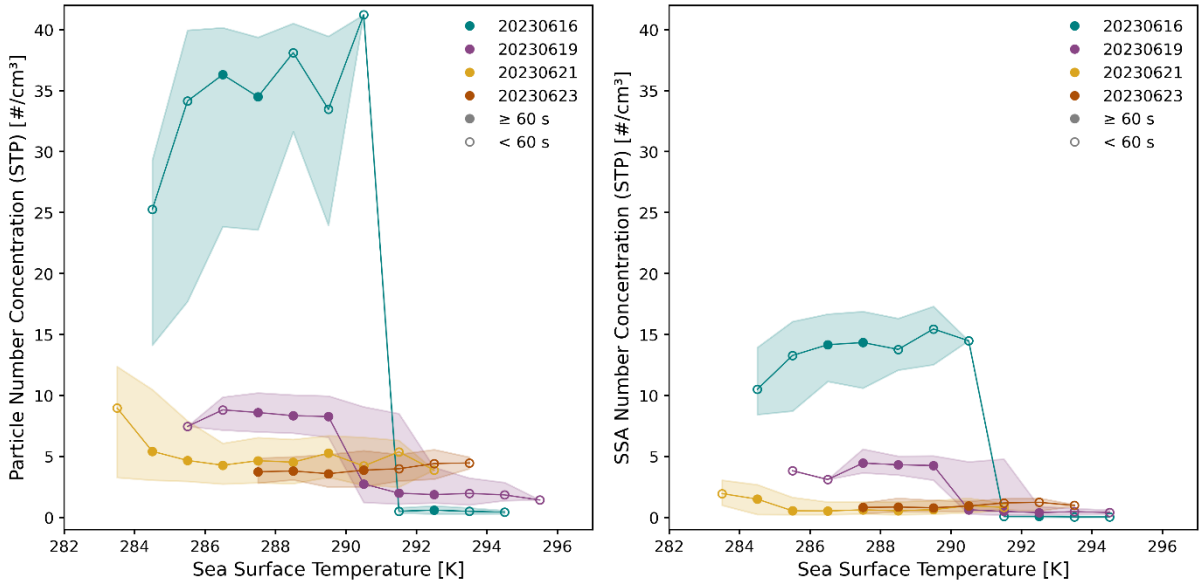

Figure 4.6: Dependence of particle number concentration (left) and SSA number concentration (right) of particles between 0.53 and 5.10 µm on wind speed. Shaded are are the 10th and 90th percentile. Empty markers indicate bins with less than 60 datapoints. The solid lines connect the datapoints to guide the eye.

4.4. Number Size Distribution

Figure 4.7 depicts the particle number size distribution measured by the CAS over the course of the periods of interest. The x-axis represents the CAS size bins with geometric means at 0.56, 0.64, 0.71, 0.91, 1.74, 3.74, 7.13 and 11.72 µm. The bin boundaries are [0.53, 0.61], [0.61, 0.67], [0.67, 0.75], [0.75, 1.11], [1.11, 2.74], [2.74, 5.10], [5.10, 9.98] and [9.98, 13.76]. Per bin, the median number concentration is indicated by the scatterplot and the error bars correspond to the 25th and 75th percentiles. The median size is non-zero for all flights for particles between 0.53 and 5.10 µm. The median at bin center 7.13 µm is only non-zero for flight 20230616, which also exhibits the highest number concentrations overall. Flights 20230616 and 20230619 show a maximum at a diameter of 0.91 µm with values of 34.77 #/cm^3 and 11.82 #/cm^3 respectively, flights 20230621 and 20230623 at 0.64 µm with values of 9.95 and 7.74 #/cm^3.

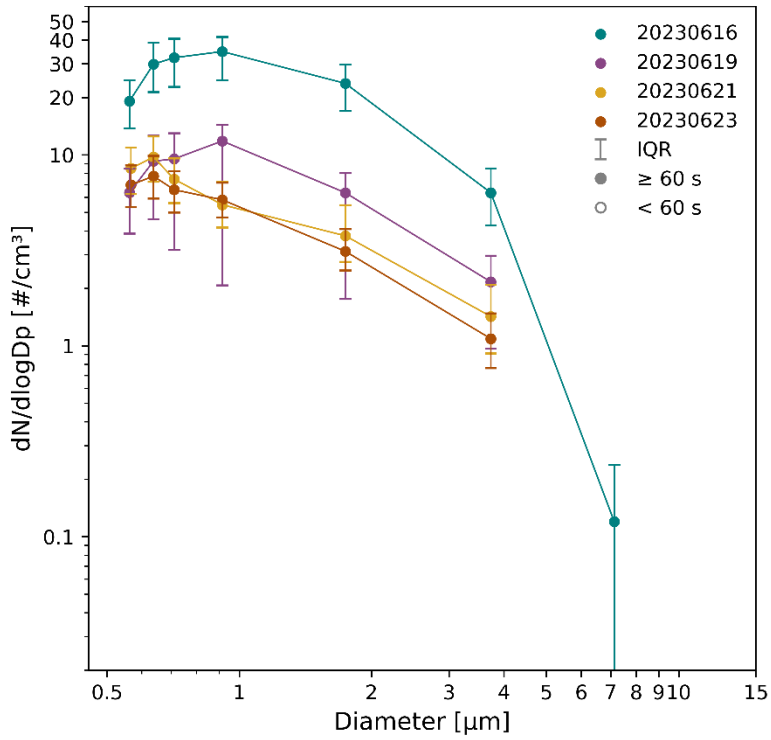

Figure 4.7: Particle number size distribution of the AEROMMA marine flights. Datapoints mark the median concentration per bin. Filled markers indicate that more than 60 values fall into the bin. Whiskers indicate the inter-quartile range. The solid lines connect the datapoints to guide the eye.

In Figure 4.8 this data is separated into three wind speed regimes, [0, 10) m/s (low), [10, 20) m/s (medium) and [20, 30) m/s (high). We observe that for low wind speeds the peak occurs at 0.64 µm for all 4 flights. In the medium wind speed regime, peaks are found at both 0.64 and 0.91 µm. For high wind speeds, data of only two flights remain, which both exhibit peaks at 0.91 µm. Consequently, the peaks shift with an increase in wind speeds from 0.64 to 0.91 µm. Analyzing the size distributions for wind speeds of 10–20 m/s and 20–30 m/s during flight 20230616 in Figure 4.8 reveals, that this decrease corresponds to a decrease of all bin values in the size distribution while maintaining the shape size distribution.

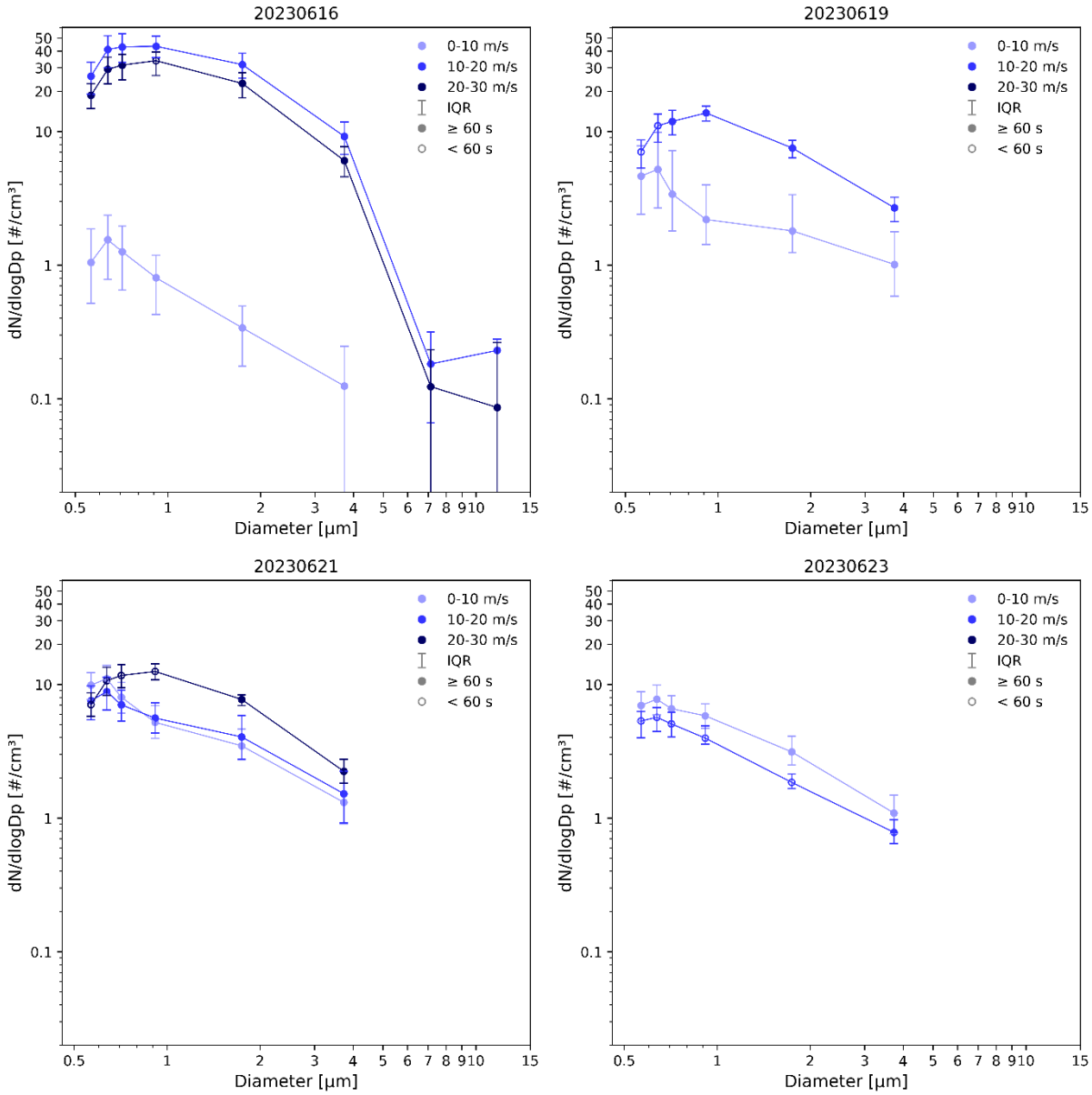

Figure 4.8: Particle number size distribution separated by flight date and plotted for three wind speed regimes. Datapoints mark the median concentration per bin. Filled markers indicate that more than 60 values fall into the bin. Whiskers indicate the inter-quartile range. The solid lines connect the datapoints to guide the eye.

5. Discussion

The following two sections will interpret and discuss the presented results in the context of the current literature on the topic. The analysis of the literature regarding SSA concentrations and their dependence on wind speed is complicated by several factors: Firstly, depending on the study, SSA is quantified using number concentration, volume concentration, mass concentration and production flux. These quantities are difficult to compare. Secondly, the reported size ranges differ considerably, which heavily impacts the values of the concentrations reported. Particles sizes are also measured and reported at varied relative humidity, usually either dry, at ambient RH or at 80% RH, which further affects the size range. Thirdly, SSA concentration, size distributions and wind speed are all affected by the altitude at which the measurements are taken. This last complication may be especially influential when comparing ship-based measurements, which happen at a height of 10–30 m above sea level, and airborne measurements, which take place in several hundred meters above sea level. Liu et al. (2021) presents a comparison of wind speed measured at 150–200 m flight altitude with ERA5 hourly 10 m wind speed in Figure S3 in the Appendix, from which they conclude that for their dataset the wind speed in 150–200 m altitude was a proxy for the 10 m wind speed. Based on this information, the following discussion compares aircraft-based measurements and ground-based measurements of wind speed and particle concentration. However, differences in wind speed at surface level and flight altitude (< 280 m) still have to be considered potentially significant when interpreting these comparisons.

5.1. General Findings

Marine Aerosol Composition

The results presented in Figure 4.4 show that only 14% of measured particles with diameters between 0.5 and 1 µm were classified as sea salt by the PALMS instrument. Even of particles with diameters between 1 and 1.5 µm only 72% contained sea salt, while almost 90% of particles between 1.5 and 4 µm contained sea salt. Consequently, it was necessary to modulate the particle number concentration measured by the CAS as described in Section 3.5 in order to be able to draw conclusions about SSA.

The high percentages of biomass burning particles measured during flight 20230621 and 20230623 are reflected in the measured CO mixing ratio: The highest median CO mixing ratios were measured during flight 20230623 with (121 ± 3) ppb, followed by flight 20230621 with (99 ± 2) ppb. The two other flights, 20230616 and 20230619, exhibited CO mixing ratios of (96 ± 2) ppb and (93 ± 2) ppb respectively. As discussed in Section 2.3.1, the CO mixing ratio

is an indicator for anthropogenic influence and biomass burning, and elevated values may indicate a continental origin of the sampled airmass. The NOAA-LGR team recommends using the CO mixing ratios reported by the Mauna Loa observatory on Hawaii as a pacific background value, which was 86 ppb (median) between the 16th and the 24th June 2023 (Andrews et al., 2023). The varying deviations from this background measured during the marine flights may suggest varying origins of the air. This is supported by HYSPLIT back trajectories, which were calculated with the specifications described in Section 3.4. The five-day back trajectories of flight 20230621 and especially 20230623 show possible air source regions in northern Canada, while the other two flights don't exhibit this. Furthermore, according to satellite data provided by the Aqua, Terra, Suomi NPP and NOAA-20 satellites there were active wildfires burning throughout June within the region in question. Figure 5.1 shows the HYSPLIT back trajectories for all 4 flight days overlayed on a NASA worldview satellite image of the 17th of June 2023. The orange dots mark fires detected by the MODIS instrument mounted on the Terra and Aqua satellites (MODIS Science Team, 2021b, 2021a), while the red dots indicate fires detected by the VIIRS instrument onboard the Suomi NPP (NASA VIIRS Land Science Team, 2020b) and NOAA-20 satellites (NASA VIIRS Land Science Team, 2020a). Several back trajectories calculated for flight 20230623 cross the region where the cluster of wildfires was burning throughout most of June, according to the 'Fire and Thermal Anomalies' data product. Flight 20230321 also exhibits back trajectories close to the region, however fewer and further away from the fires. The other two flights do not exhibit any back trajectories in that area. More detailed plots of HYSPLIT back trajectories are available in Figures A.5–A.9 in the Appendix.

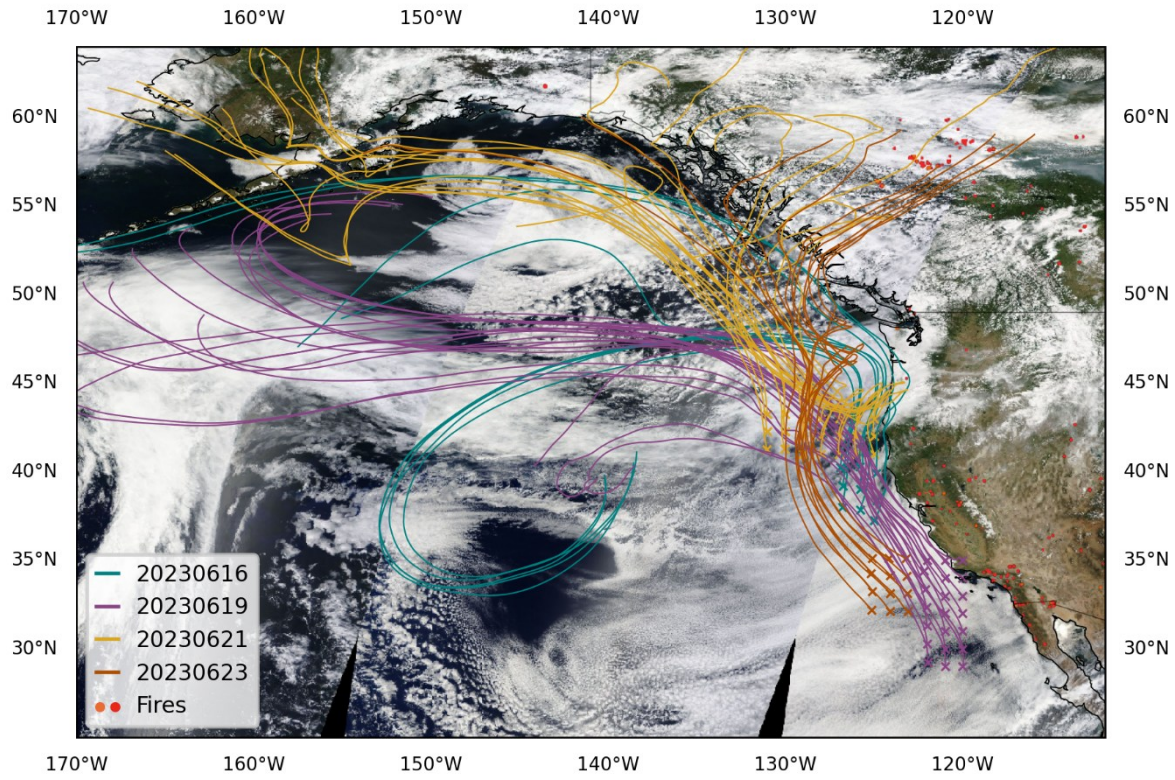

Figure 5.1: NASA Worldview Snapshot of the Terra/MODIS Corrected Reflectance (June 17th 2023, https://wvs.earthdata.nasa.gov), overlayed with HYSPLIT trajectories (lines) and the 'Fire and Thermal Anomalies' data product by the MODIS instrument onboard the Terra and Aqua satellites (orange markers) and the VIIRS instrument onboard the Suomi NPP and NOAA-20 satellites (red markers). The data product marks fires and other thermal anomalies such as volcanoes and gas flares.

An influence of Canadian wildfires on the measurements during the AEROMMA marine flights is a possible explanation for the elevated CO values, as well as the high biomass burning contributions to the accumulation mode of flight 20230621 and 20230623.

SSA Concentration

The range of particle and SSA number concentration during the periods of interest of the AEROMMA campaign was 0.72–43.19 #/cm^3 and 0.00–29.17 #/cm^3 respectively. This matches the order of magnitude of the reported typical concentrations of sea salt in the atmosphere, which have been estimated to be 5–30 #/cm^3 (Blanchard & Cipriano, 1987; O'Dowd & Smith, 1993 as cited in Seinfeld & Pandis, 1998). While the SSA concentrations reported in this thesis fall into the order of magnitude reported in literature, the four marine flights do not exhibit a consistent trend, except for very low wind speeds. At wind speeds lower than 10 m/s, the concentration holds constant near 0 for all four flights, which may partly be explained by the presence clouds: Although measurements in clouds and periods of less than 10 s between clouds were excluded by applying the cloud flag, Figure 5.2 shows two instances in which the

SSA number concentration is lowered relative to the rest of the flight if there were several clouds flagged around the measurement:

- The period 00:00–02:00 UTC during flight 20230616 exhibits SSA concentrations close to 0 #/cm^3 and several occurrences of clouds, while the rest of the flight was cloud free and exhibited the highest concentrations of all flights, between 10 and 20 #/cm^3.
- During flight 20230619, SSA concentrations of approximately 5 #/cm^3 were sampled for the most part, except between ca. 19:50 and 22:00 UTC, during which the concentration dropped to below 2 #/cm^3. While there were instances of clouds throughout flight 20230619, they were visibly denser during this period.

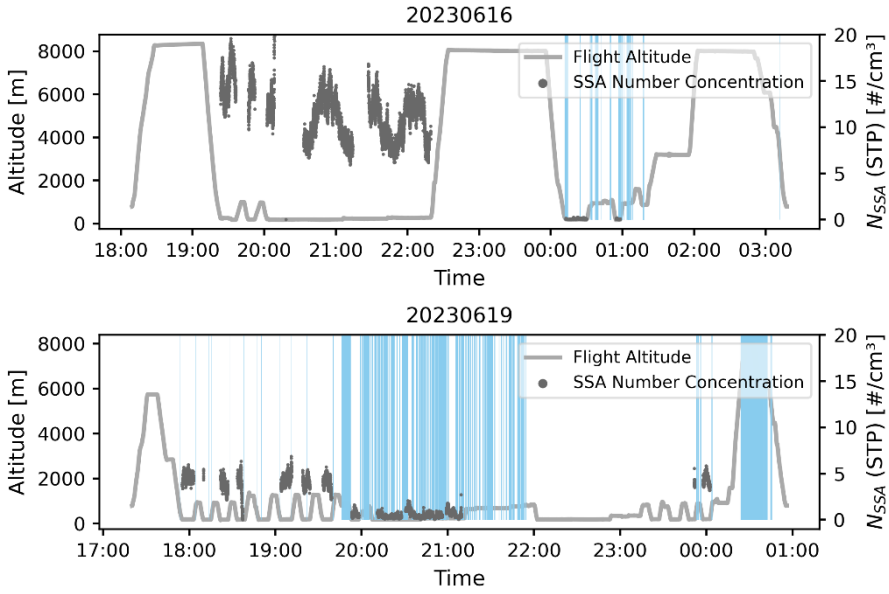

Figure 5.2: Timeseries of flight altitude and SSA number concentration for two of the marine flights. The vertical blue lines indicate instances where the cloud flag was 1.

The frequency of cloud flags indicate that these regions were overall cloudy while NASA DC-8 was in the area. Thus, nucleation scavenging and/or impaction scavenging may have been a major factor affecting the aerosol number concentration measured in the regions, which is expected (Murphy et al., 2019; Shinozuka et al., 2004; Zheng et al., 2018). Murphy et al. (2019) found that SSA was effectively removed over their entire measurement range, which was 0.3–3 µm. They conclude that this suggests nucleation scavenging as the dominant removal mechanism, since impaction scavenging would affect coarse-mode particles more than submicron particles. The low concentration between 00:00 and 02:00 UTC during flight 20230616 (Figure 5.2, top) and ca. 19:50 to 22:00 UTC during flight 20230619 (Figure 5.2, bottom) may thus be explained by the formation and presence of clouds. This offers a possible explanation of the rapid increase in number concentration at ca. 10 m/s of flights 20230616 and 20230619. Although flights 20230621 and 20230623 also exhibit cloudy periods, it was

not possible to identify a concurrent drop in measured number concentration due to the overall low concentrations. Furthermore, it was attempted to find a proxy for clouds, which may also affect aerosol number concentration if they are located in a higher atmospheric layer than the measurement. The nitrogen dioxide (NO_2) photolysis rate jNO_2, provided by the J-CAFS instrument of the Forschungszentrum Jülich (Bohn & Lohse, 2017) was briefly examined for this. It quantifies the rate at which NO2 decays due to solar radiation, which could indicate the presence or lack of clouds above the aircraft flight track. The variable jNO_2 is shown in Figures A.1–A.4 in the Appendix, however based on a brief examination of the forward video of the DC-8, it was not possible to identify a consistent positive or negative correlation between cloudiness and NO_2 photolysis rate. Further analysis of the relationship between SSA concentration and jNO_2 would be beneficial, but is beyond the scope of this thesis.

As mentioned previously, the flights do not show a consistent relationship between SSA number concentration and wind speed. The aspect sticking out the most is flight 20203616, which exhibits a decrease in number concentration for wind speeds greater 10 m/s as well as peak concentrations four times higher than the peak number concentrations of the other flights. This period of flight 20230616 will be analyzed in detail in Section 5.2.

Recent studies analyzing the relationship between SSA number concentration and wind speed in a similar size range are presented in Figure 5.3. Zheng et al. (2018) reported concentrations up to 30 #/cm^3 and Saliba et al. (2019) found concentrations up to 50 #/cm^3. Both studies find a rapid increase of SSA concentration with wind speed, as pictured in Figure 5.3. Note, that Saliba et al. (2019) reports rather high concentrations despite the fact that the authors considered only dry particles greater than 0.6 µm. Flores et al. (2021) reports concentrations of < 5 #/cm^3 in a similar size range (Flores et al., 2021).

Table 5.1: Overview of studies on the relationship between SSA concentrations and wind speed.

Study	Research Platform	Reported diameter	Reported size range
Saliba et al. (2019)	Cruise	dry mobility diameter	0.6–5 µm
Zheng et al. (2018)	Station	details not explicitly stated, but likely dry optical diameter	> 0.3 µm
Pant et al. (2008)	Cruise	diameter at 80% RH	0.5–20 µm
Flores et al. (2021)	Cruise	dry optical diameter	> 0.58 µm

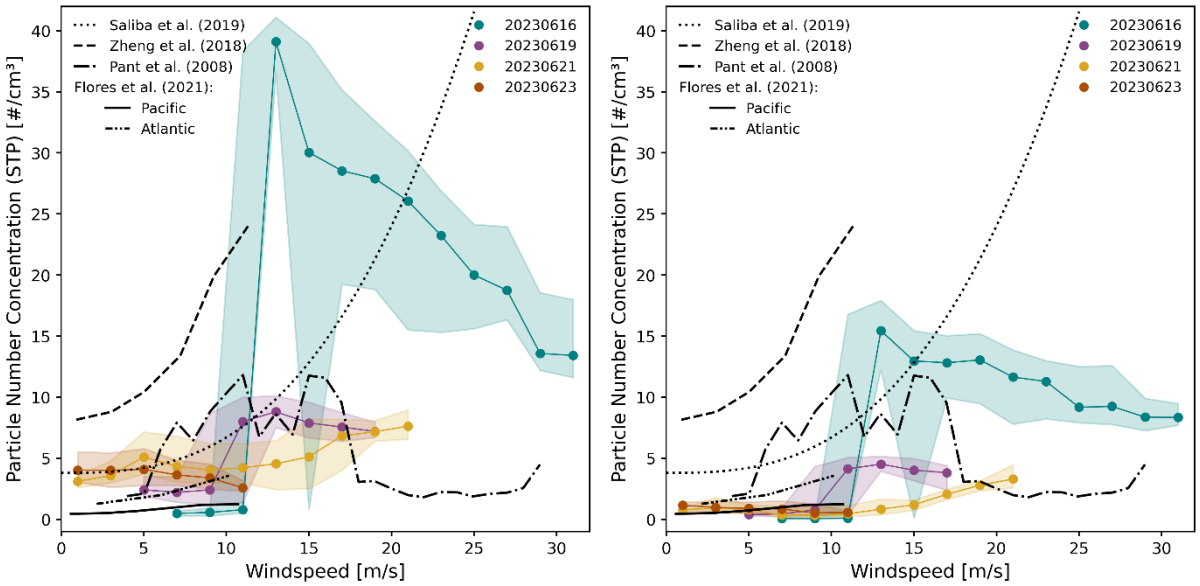

Figure 5.3: AEROMMA data of particle number concentration (left) and SSA number concentration (right) plotted against wind speed. Wind speed bins are 2 m/s, points mark the median and the shaded areas correspond to the 10th and 90th quantiles. The solid lines connect the datapoints to guide the eye. In both plots, SSA number concentration vs. wind speed relationships of four studies are overlayed.

Flores et al. (2021) does not confirm the strong increase of SSA concentration with wind speed. The authors found a stronger correlation between SSA concentration in the Atlantic than the Pacific, however both exhibit comparatively low concentrations. Their trend found in the Pacific resembles the data acquired in cloudy regions during the AEROMMA campaign at wind speeds smaller than 10 m/s. The only study reporting a relationship between SSA concentration and wind speed that is not monotonously increasing is Pant et al. (2008). They report a sudden increase in concentrations at ca. 5 m/s and a sudden decrease at ca. 17 m/s. The authors propose that the decrease in concentration at high wind speeds may be due to the scavenging of aerosol particles by droplets ejected at high wind speeds. However, they also note that their sampling efficiency of large particles may not have been isokinetic at high wind speeds. The AEROMMA concentrations partly exhibit a similar sudden increase around ca. 10 m/s, however as discussed previously, this may be due to cloudy sampling regions. Furthermore, the AEROMMA concentrations show a levelling off and slight decrease for high wind speeds, but no sharp decrease as presented in Pant et el. (2008). Overall, there is a difference of up to one order of magnitude between the concentrations reported by the studies listed above. The concentrations measured during the AEROMMA campaign fall into the general range presented in literature, but don't match up with any of the studies.

Some of the variation in the literature regarding the relationship between SSA concentration and wind speed may be explained by reasons listed in the very beginning of the discussions,

namely the differences in reported size ranges, diameter and acquisition height. However, Lewis & Schwartz (2004) also suggest that wind speed alone may not be a suitable parameter to describe SSA concentration. The authors suggest that gustiness and steadiness of the wind may have a significant impact on SSA production. This is supported by the findings of Callaghan et al. (2008), which found an impact of wind history on whitecap fraction: The authors found that whether the wind speed in the 2.5 hour before measurement increased or decreased affected the whitecap fraction at a given wind speed at the time of measurement.

There's no discernible trend in the relationship between SSA concentration and SST within AEROMMA data. Overall, the SSA concentration shows little dependence on SST. Two flights, 2020616 and 20230619 exhibit a sudden decrease in concentration with increasing SST, while 20230621 and 20230623 show no dependence of SSA concentration of SST. The decrease may be explained by the occurrences of clouds discussed previously. However, because the SST data has several time periods where no data is available, several SST bins contain fewer than 60 datapoints, as indicated by the empty markers in Figure 4.6. While the parameter SST is still debated in literature, a consensus on a positive relationship seems to have emerged in the last years. Liu et al. (2021) summarizes the current state of the literature and presents data supporting a positive correlation. The paper suggests a stronger relationship between SSA volume concentration and SST at higher wind speeds. The authors also report a stronger influence of both wind speed and SST on the abundance of larger particles. Although Liu et al. (2021) has brought significantly more insight on the controlling factors of SSA abundance, more evidence to support their conclusions is needed. This thesis does not support the hypothesis that SSA concentration increases with increasing SST, however the range of sea surface temperature is rather small compared to the data presented in the literature. During the AEROMMA campaign, a range of ca. 12 K was measures, while e.g. Liu et al. (2021) reports a spread of ca. 30 K.

Particle Number Size Distribution

The results presented in this thesis show a shift in the peak of the particle number size distribution with an increase in wind speeds from 0.64 to 0.91 µm ambient diameter (Figure 4.8). Median number concentrations are zero for all size bins > 13.76 µm. As described in Section 2.4.1, the film droplet peak is expected between at a diameter of 0.2 and 1 µm at 80% RH (Veron, 2015). Jet and spume droplet modes are expected at ca. 10 and 200 µm respectively. Consequently, we likely have measured mostly film droplets. Given that we know that the particles with ambient diameters between 0.5 and 1 µm are mostly sulfate/organic/nitrate and biomass burning particles, the increase in concentration for larger bin sizes may be due to an increase in SSA production. Interestingly, we don't observe a

decrease in concentration in particles < 1 µm for increasing wind speeds, which indicates that wind did not act as a dilution mechanism during these measurements. Furthermore, the decrease in total number concentration during flight 20230616 over the entire range of sizes indicates that decrease is not due to a variation of RH, which would shift the size distribution. It's also likely not due to the removal mechanism suggested by Pant et el. (2008), which would affect larger particles more than smaller ones due to their larger impaction cross section. Instead, it may indicate a removal mechanism that affects particles of all measured sizes similarly. This will be discussed further in Section 5.2.

The particle number size distribution of the Atmospheric Tomography Mission (Atom) campaign reported by Liu et al. (2021) is plotted together with the particle number size distribution of the marine flights in Figure 5.4. At low wind speed, the size distribution exhibits its mode at 0.24 µm and a secondary maximum at 0.47 µm dry diameter. With increasing wind speed, the secondary maximum increases in magnitude while the mode concentration decreases, similarly to the behavior of the AEROMMA size distribution. Note that the resolution of the ATom size distribution is much higher than the resolution of the size distribution presented in this thesis. Furthermore, Liu et al. (2021) reports dry diameters and consequently their size distribution is expected to be shifted towards smaller particle sizes. Unfortunately, the ambient RH data of the ATom size distributions is not available, thus it was not possible to estimate the ambient size distribution accurately. However, we can calculate a range of realistic values using the formula for the hygroscopic growth factor presented in Section 3.5. Assuming standard temperature (0°C) and the range of RH measured during the AEROMMA campaign (49–97%), we calculate the following:

Table 5.2: Conversion of dry diameters (in µm) measured by Liu et al. (2021) during the ATom campaign to RH values measured during the periods of interest of the AEROMMA campaign, which ranged between 49 and 97%. The median value of the periods of interest of the AEROMMA campaign was 83%.

Dry diameter reported by Liu et al. (2021)	Calculated to 49% RH (minimum)	Calculated to 83% RH (median)	Calculated to 97% RH (maximum)
0.24 µm	0.31 µm	0.44 µm	0.69 µm
0.47 µm	0.60 µm	0.87 µm	1.38 µm

Consequently, the two occurring maxima of the AEROMMA size distributions, 0.64 and 0.91 µm fall into the possible ranges of the ambient maxima measured by Liu et al. (2021), meaning that the AEROMMA peaks may correspond to the ATom peaks. However, the range of realistic RH values is chosen very broadly here and we have no information of the true ambient conditions during the ATom measurements.

Note that the analysis presented in Liu et al. (2021) excludes particles smaller than 0.5 µm dry diameter to exclude non-marine aerosol sources.

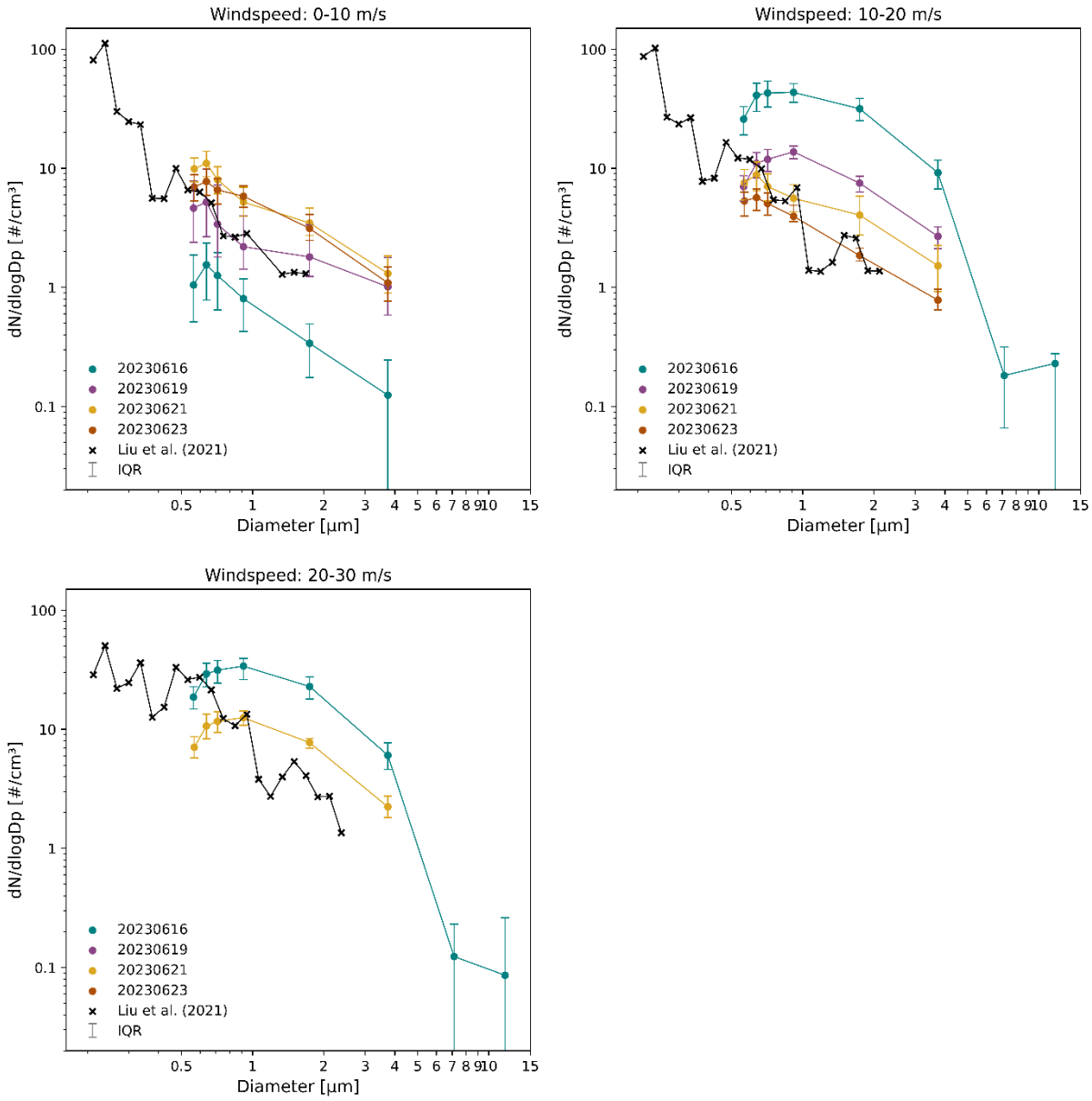

Figure 5.4: Particle number size distribution of the AEROMMA marine flights (periods of interest) plotted together with the ATom size distribution (150-200 m altitude above water, excl. periods associated with precipitation, RH < 50 % and sea salt volume fractions < 50 %) provided by Liu et al. (2021) for different ranges of wind speed (upper left: 0-10 m/s, upper right: 10-20 m/s and lower left: 20-30 m/s). Diameters are ambient for the AEROMMA data and dry for the ATom data. Markers indicate the median value per bin for both AEROMMA and ATom data, the solid lines connect the datapoints to guide the eye. Whiskers indicate the inter-quartile range.

5.2. Case Study

As described in the previous section, flight 20230616 differs substantially from the other marine flights. Figure 5.5 shows that flight 20230616 sampled air at two different locations. The southern part (marked blue) exhibited low wind speeds and number concentrations with no

discernible relationship between the two, whereas the northern part (marked red) experienced the highest wind speeds and number concentration of all the flights. Furthermore, the relationship between number concentration and wind speed is negative.

The bottom subplot in Figure 5.5 depicts the altitude profile, with northern and southern part marked red and blue respectively. The vertical lines in light blue mark occurrences of clouds and any periods between clouds < 10 s. We observe that while there were no occurrences of clouds in the northern part, there were several in the southern part, which may explain the low concentration measured there, as discussed in the previous section.

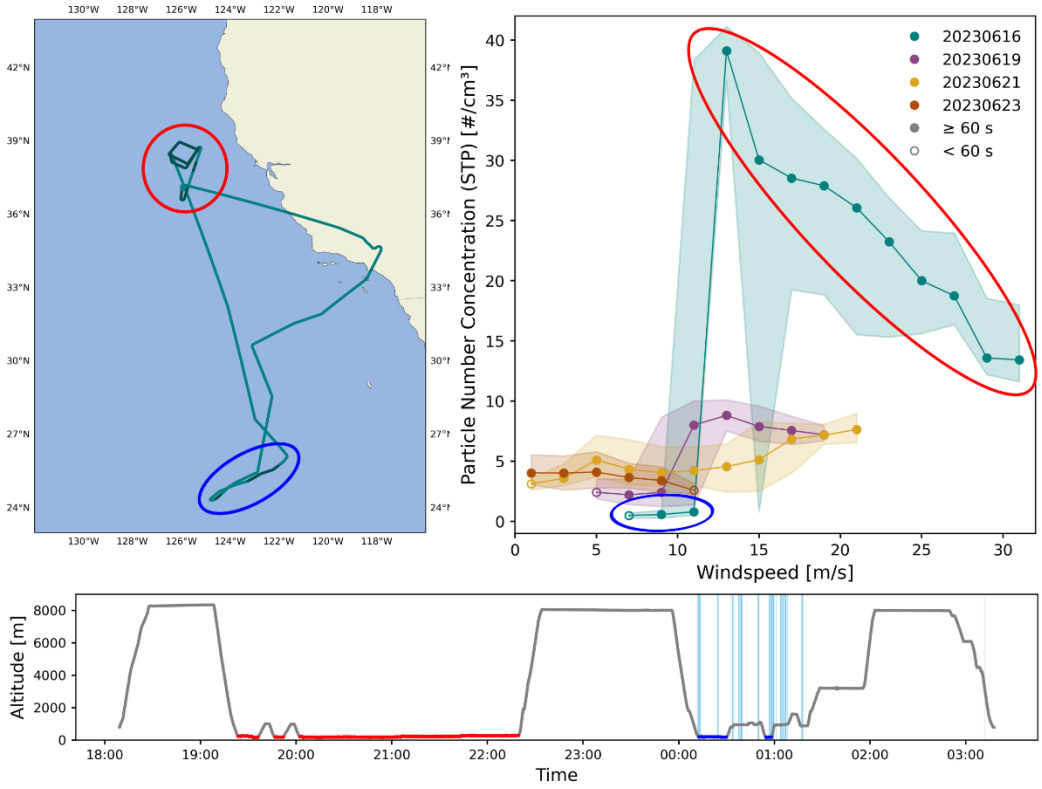

Figure 5.5: Upper left: Flighttrack of flight 20230616. Darker colors correspond to data fulfilling the constraints. Upper right: Particle number concentration (ambient diameters between 0.53 and 5.10 µm) vs wind speed. Bottom: Timeseries of altitude profile. Vertical stripes in light blue mark occurrences of clouds (cloud flag = 1). In all subplots, red and blue mark the northern and southern part of the flight track respectively.

To further analyzes flight 20230616, specifically the northern part, Figure 5.6 depicts a closeup of the flight track in this region on a map (top), as well as a closeup of the timeseries of altitude (bottom). Both are color coded by particle number concentration. Note, that the box we see on the map was flown three times at three different altitudes, as visible in the timeseries. On the map, this is not distinguishable because the boxes were flown exactly above each other, however the color code (i.e. particle number concentration) oscillates similarly for each box. The timeseries also shows manually defined periods of the peak number concentration (highs, marked dark grey) and lowest number concentrations (lows, marked light grey) per oscillation.

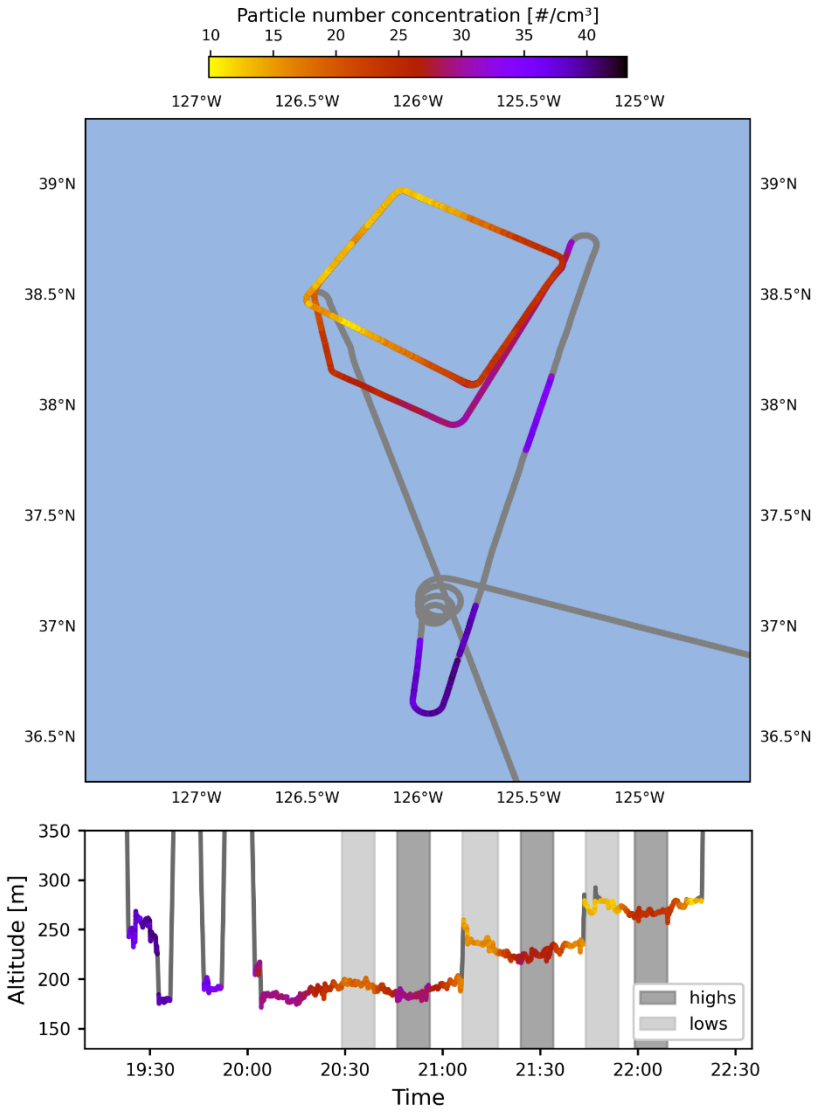

Figure 5.6: Top: Flight track of northern part of flight 20230616, color coded by particle number concentration. Bottom: Timeseries of the altitude profile of this part of the flight, also color coded by particle number concentration. Periods at the peak of the oscillations in particle number concentration were defined as 'highs' and marked in dark grey, periods at the bottom were defined as 'lows' and marked in light grey.

The Figure illustrates that the oscillation of particle number concentration in this region is due to a local variation in aerosol burden. The south-eastern leg of the box exhibits higher particle number concentration than the north-western leg. The three periods southern of the box, between 19:00 and 20:00 UTC, exhibit even higher concentrations.

The oscillation in particle number concentration is also present after the modulation by sea salt fraction, in the SSA number concentration. To show this, Table 5.3 contains the median value of 6 variables for the highs, the lows and the ratio between the median of the highs and lows. The median particle number concentration was 26.44 #/cm^3 during the highs and 15.86 #/cm^3 during the lows, which correspond to a highs/lows ratio of 1.67. The SSA number concentration exhibits lower absolute values, but still has a highs/lows ratio of 1.55. Thus, the oscillation in

SSA number concentration is still present, although it may be slightly reduced due to a weak anti-correlation with sea salt number fraction, for which the highs/lows ratio is 0.91. While the relative humidity does show variations between ca. 75% and 95% in the region, as is visible in Figure 4.3, this variation does not match the oscillation in aerosol number concentration.

Table 5.3: Median values of particle number concentration, SSA number concentration, sea salt fraction, wind speed, relative humidity and CO elevation above background for the previously defined 'high' periods and 'low' periods. The ratio of the median of the 'highs' and the median of the 'lows' is also listed.

Variable	Median (lows)	Median (highs)	Ratio of medians highs/lows
Particle number concentration [#/cm^3]	15.84	26.40	1.67
SSA number concentration [#/cm^3]	8.17	12.60	1.55
Sea salt fraction [%]	53	50	0.91
Wind speed [m/s]	26	21	0.80
Relative humidity [%]	88	86	0.98
CO (elevation above background) [ppb]	6	11	1.93

The CO mixing ratio however shows a strong oscillation matching the number concentration. This is not well reflected by the highs/lows ratio of the absolute values because the CO background is rather high relative to the local variability. The NOAA-LGR team recommends using the CO mixing ratios reported by the Mauna Loa observatory on Hawaii as a pacific background value, which was 86 ppb (median) between the 16th and the 24th June 2023 (Andrews et al., 2023). Median absolute values of 92 ppb for the lows and 97 ppb for the highs result in elevations above the background of 6 ppb and 11 ppb respectively, and a highs/lows ratio of 1.79. HYSPLIT back trajectories are shown in Figure 5.7 and support the suspicion that airmasses of different origins were sampled. The purple and pink trajectories ending in the eastern part of the grid likely have travelled along the coast of most of the north American continent, where they may have been influenced by human activity and the wildfires which occurred at the time in Canada, as discussed in the previous section. The more western trajectories show a history of the air further away from the coast with less time spent in coastal regions.

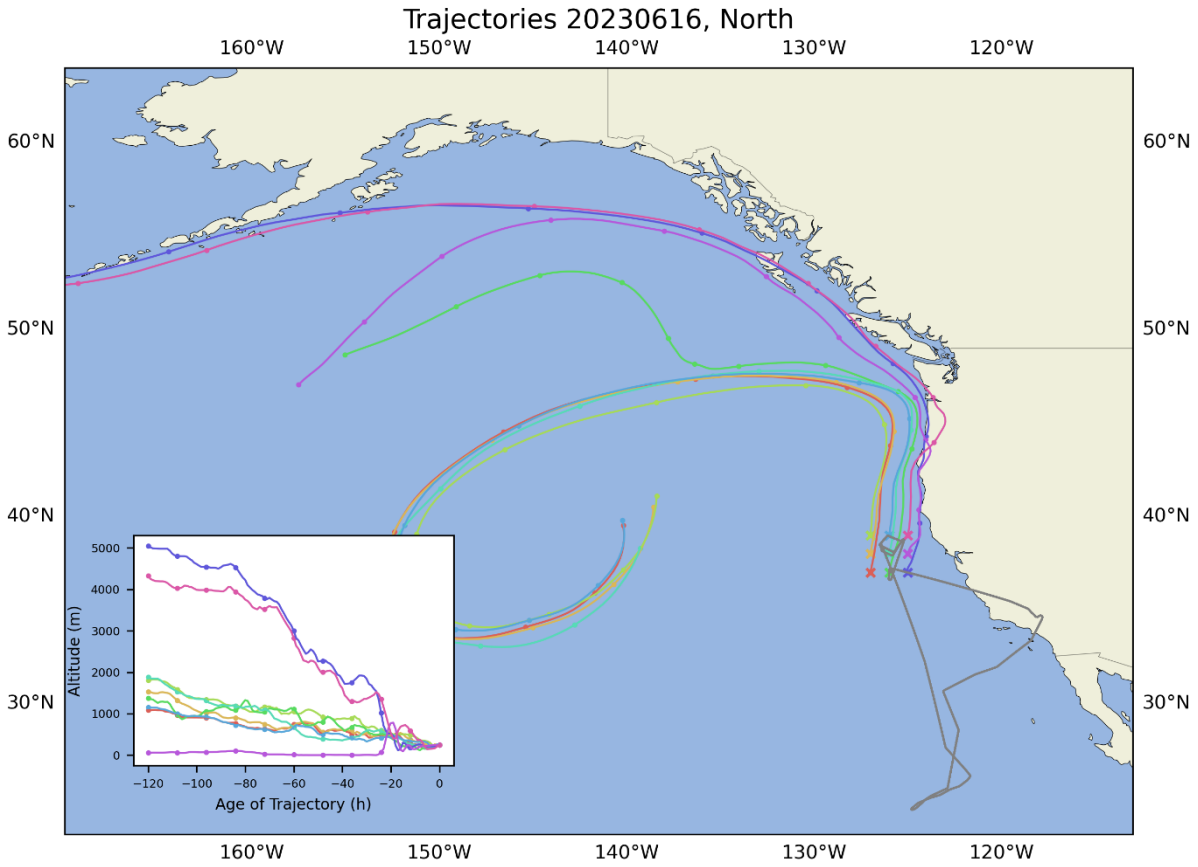

Figure 5.7: Map of flight track of flight 20230616 (grey line). Colorful lines show the HYSPLIT back trajectories with the starting point marked by 'x'. Back trajectories are marked with a dot every twelve hours. Inset plot: Altitude profiles of back trajectories.

Despite the indications that different airmasses were sampled during the ‘highs’ and ‘lows’ periods, this thesis cannot conclude that any particular influence is responsible for the distinct difference in SSA number concentrations of these periods. Although the CO values may indicate a possible continental influence, the high relative humidity and sea salt fraction contradict this. It should be noted that an increased CO value may be due to an influence of a continental airmass, but that this does not imply the presence of aerosol particles. As discussed in the previous section, wind history and wind gustiness may have an effect on SSA concentration that was not quantified in this thesis. Furthermore, no investigation into potential past rainfall has been made, which would be a strong removal mechanism of SSA particles, in particular of large particles. However, the decrease in number concentration across all sizes, as pictured in Figure 5.8, may indicate a removal factor that effectively removes particles of all measured sizes. Murphy et al. (2019) suggests that nucleation scavenging is such a removal mechanism. Consequently, further investigation into the presence and formation of clouds in this region, both at the time of sampling and before, is needed.

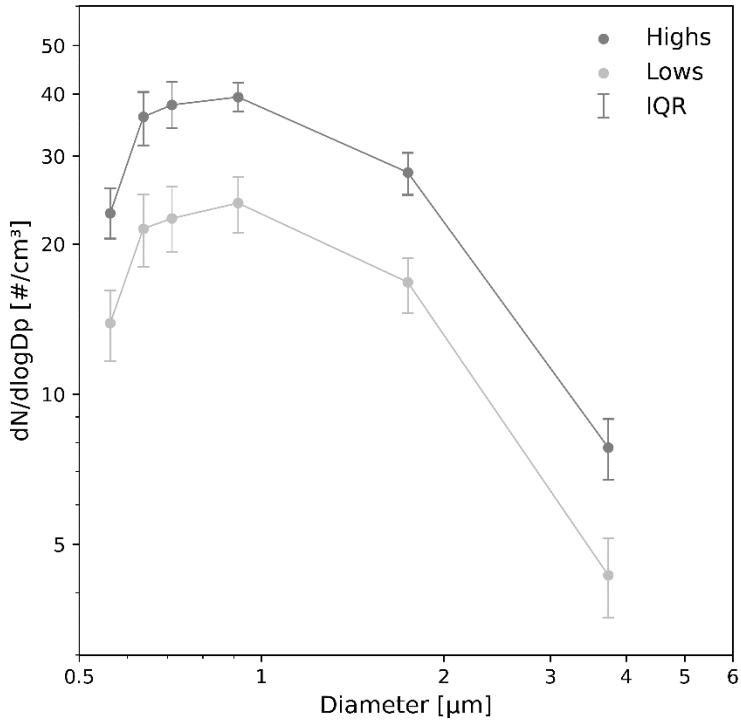

Figure 5.8: Particle number size distribution during the previously defined highs and lows in particle concentration. Datapoints mark the median number concentration per bin, whiskers indicate the inter-quartile range. The solid lines connect the datapoints to guide the eye.

6. Conclusions

This thesis analyzed data on aerosol concentration, size distribution and composition collected during four research flights of the AEROMMA campaign, conducted mostly in the pacific MBL. The main objectives were to study the impact of wind speed (1–31 m/s) and SST (283–295 K) on SSA concentrations and total particle size distribution. Furthermore, the measured aerosol composition was investigated in order to filter out non-SSA aerosol species from the SSA analysis.

The analysis of the AEROMMA marine flights showed that 90% of the aerosol particles of ambient particle diameter above 1.5 µm were classified as sea salt by the PALMS instrument. However, the particle composition between 0.5 and 1.5 was impacted by sulfate/organic/nitrate particles and biomass burning particles. This biomass burning influence was particularly prominent in particles between 0.5 and 1 µm during the two flights conducted on the 21st and 23rd of June: Ca. 30% and 40% of 0.5–1 µm particles measured during flight 20230621 and 20230623 respectively were attributed to biomass burning. HYSPLIT back trajectories suggest that this influence originated in Canadian wildfires. This illustrates that aerosol measured in marine environments is not necessarily dominated by sea salt, even hundreds of kilometers away from the nearest coastline. If no data on aerosol composition is available, the analysis of the marine aerosol composition presented in this thesis indicates that particles larger than 1.5 µm ambient diameter could be used when studying the influence of wind speed and SST on the SSA number concentration. This could help ensure that the majority of the particles measured are indeed SSA particles.

The non-SSA influences on the marine aerosol concentration were filtered out as best as possible by modulating the total aerosol number concentration with the sea salt fraction measured by the PALMS instrument. The resulting SSA number concentration was found to be higher at wind speeds above 10 m/s than below, but did not exhibit the steady positive dependence on wind speed that's expected based on previous studies. The SSA concentration for windspeeds below 10 m/s was < 3 #/cm^3 for all flights, which may partly be due to the presence of clouds in the sampling region. At a wind speed of ca. 10 m/s, an increase in SSA concentration occurred for three out of four flights. At windspeeds higher than ca. 10 m/s, there was no consistent relationship between SSA concentrations and windspeed. During one flight, no wind speeds > 10 m/s were measured. The increase in SSA number concentration at ca. 10 m/s was also reflected by a change in shape in the measured particle number size distributions, which takes into account all aerosol species.

Furthermore, no consistent relationship between SSA concentration and SST was identified in this analysis. The range of SST during the AEROMMA marine flights was 12 K, which is significantly less than in other studies. This may be part of the reason why no dependence was observed.

Flight 20230616 exhibited an unexpected behavior due to a high number concentration that decreased with increasing windspeed. A case study was conducted to investigate this decrease, which concluded that the sampling occurred at the boundary between two distinct airmasses with different histories. The particle number size distributions in these two airmasses exhibited the same shape at different concentration levels, which suggests that additional analysis of possible dilution by particle-free air and removal mechanisms, particularly nucleation scavenging, is needed.

Future work should further investigate removal mechanisms of SSA, such as the formation of clouds and precipitation prior to or during the measurement. In general, the abundance of SSA in our atmosphere and its dependence on wind speed and SST remain poorly constrained and require further research. Most studies investigating this topic rely on short-term campaign-based measurements, hence studies analyzing long-term measurement series would be of value to the scientific debate. Furthermore, the effect of wind history, steadiness and sea state on SSA burden needs additional research.

Bibliography

AEROMMA. (n.d.). NOAA Chemical Sciences Laboratory. Retrieved July 15, 2024, from https://csl.noaa.gov/projects/aeromma/

AEROMMA Goals. (n.d.). NOAA Chemical Sciences Laboratory. Retrieved July 15, 2024, from https://csl.noaa.gov/projects/aeromma/science/goals.html

AEROMMA Platform: NASA DC-8. (n.d.). NOAA Chemical Sciences Laboratory. Retrieved July 15, 2024, from https://csl.noaa.gov/projects/aeromma/dc8/

AEROMMA Platform: NASA DC-8 Payload. (n.d.). NOAA Chemical Sciences Laboratory. Retrieved August 13, 2024, from https://csl.noaa.gov/projects/aeromma/dc8/payload.html

Andrews, A., Crotwell, A., Crotwell, M., Handley, P., Higgs, J., Kofler, J., Lan, X., Legard, T., Madronich, M., McKain, K., Miller, J., Moglia, E., Mund, J., Neff, D., Newberger, T., Petron, G., Turnbull, J., Vimont, I., Wolter, S., & NOAA Global Monitoring Laboratory. (2023). *NOAA Global Greenhouse Gas Reference Network Flask-Air PFP Sample Measurements of CO at Tall Tower and other Continental Sites, 2005-Present [Data set]* (Version 2023-08-23) [Dataset]. NOAA GML. https://doi.org/10.15138/C1VT-5507

Baumgardner, D., Jonsson, H., Dawson, W., O'Connor, D., & Newton, R. (2001). The cloud, aerosol and precipitation spectrometer: A new instrument for cloud investigations. *Atmospheric Research*, *59–60*, 251–264. https://doi.org/10.1016/S0169-8095(01)00119-3

Blanchard, D. C., & Cipriano, R. (1987). Biological regulation of climate. *Nature*, *330*(6148), 526–526. https://doi.org/10.1038/330526a0

Bohn, B., & Lohse, I. (2017). Calibration and evaluation of CCD spectroradiometers for ground-based and airborne measurements of spectral actinic flux densities. *Atmospheric*

Measurement Techniques, *10*(9), 3151–3174. https://doi.org/10.5194/amt-10-3151-2017

Boucher, O. (2015). *Atmospheric Aerosols: Properties and Climate Impacts*. Springer Netherlands. https://doi.org/10.1007/978-94-017-9649-1

Boucher, O., Randall, D., Artaxo, P., Bretherton, C., Feingold, G., Forster, P., Kerminen, V.-M., Kondo, Y., Liao, H., Lohmann, U., Rasch, P., Satheesh, S. K., Sherwood, S., Stevens, B., & Zhang, X.-Y. (2013). Clouds and Aerosols. In *Climate Change 2013: The Physical Science Basis. Contribution of Working Group I to the Fifth Assessment Report of the Intergovernmental Panel on Climate Change* (Stocker, T.F., D. Qin, G.-K. Plattner, M. Tignor, S.K. Allen, J. Boschung, A. Nauels, Y. Xia, V. Bex and P.M. Midgley (eds.)). Cambridge University Press.

Bruch, Wi., Bruch, W., Yohia, C., Tulet, P., Limoges, A., Sutherland, P., Eijk, A. M. J. V., Missamou, T., & Piazzola, J. (2023). *Atmospheric Sea Spray Modeling in the North-East Atlantic Ocean using Tunnel-Derived Generation Functions and the SUMOS Cruise Dataset* [Preprint]. Preprints. https://doi.org/10.22541/essoar.167689973.33141884/v1

Callaghan, A., de Leeuw, G., Cohen, L., & O'Dowd, C. D. (2008). Relationship of oceanic whitecap coverage to wind speed and wind history. *Geophysical Research Letters*, *35*(23). https://doi.org/10.1029/2008GL036165

Carslaw, K. S., Gordon, H., Hamilton, D. S., Johnson, J. S., Regayre, L. A., Yoshioka, M., & Pringle, K. J. (2017). Aerosols in the Pre-industrial Atmosphere. *Current Climate Change Reports*, *3*(1), 1–15. https://doi.org/10.1007/s40641-017-0061-2

de Leeuw, G., Andreas, E. L., Anguelova, M. D., Fairall, C. W., Lewis, E. R., O'Dowd, C., Schulz, M., & Schwartz, S. E. (2011). Production flux of sea spray aerosol. *Reviews of Geophysics*, *49*(2). https://doi.org/10.1029/2010RG000349

de Leeuw, G., Guieu, C., Arneth, A., Bellouin, N., Bopp, L., Boyd, P. W., van der Gon, H. A. C. D., Desboeufs, K. V., Dulac, F., Facchini, M. C., Gantt, B., Langmann, B., Mahowald, N. M., Marañón, E., O'Dowd, C., Olgun, N., Pulido-Villena, E., Rinaldi, M., Stephanou, E. G., & Wagener, T. (2014). Ocean–Atmosphere Interactions of Particles. In P. S. Liss & M. T. Johnson (Eds.), *Ocean-Atmosphere Interactions of Gases and Particles* (pp. 171–246). Springer. https://doi.org/10.1007/978-3-642-25643-1_4

Dentener, F., Kinne, S., Bond, T., Boucher, O., Cofala, J., Generoso, S., Ginoux, P., Gong, S., Hoelzemann, J. J., Ito, A., Marelli, L., Penner, J. E., Putaud, J.-P., Textor, C., Schulz, M., van der Werf, G. R., & Wilson, J. (2006). Emissions of primary aerosol and precursor gases in the years 2000 and 1750 prescribed data-sets for AeroCom. *Atmospheric Chemistry and Physics*, *6*(12), 4321–4344. https://doi.org/10.5194/acp-6-4321-2006

Diskin, G. S., Podolske, J. R., Sachse, G. W., & Slate, T. A. (2002). Open-path airborne tunable diode laser hygrometer. *Diode Lasers and Applications in Atmospheric Sensing*, *4817*, 196–204. https://doi.org/10.1117/12.453736

Dollner, M. (2022). *Assessment of the global distribution of coarse-mode aerosol and clouds with large-scale in situ aircraft observations*. https://doi.org/10.25365/thesis.72087

Dollner, M., Gasteiger, J., Schöberl, M., Gattringer, A., Beres, N. D., Bui, T. P., Diskin, G., & Weinzierl, B. (2024). The *Cloud Indicator*: A novel algorithm for automatic detection and classification of clouds using airborne in situ observations. *Atmospheric Research*, *308*, 107504. https://doi.org/10.1016/j.atmosres.2024.107504

Draxler, R. R. (1999). *HYSPLIT4 user's guide*. NOAA Tech. Memo. ERL ARL-230, NOAA Air Resources Laboratory.

Draxler, R. R., & Hess, G. D. (1997). *Description of the HYSPLIT_4 modeling system*. NOAA Tech. Memo. ERL ARL-224, NOAA Air Resources Laboratory.

Draxler, R. R., & Hess, G. D. (1998). An Overview of the HYSPLIT_4 Modelling System for Trajectories, Dispersion, and Deposition. *Australian Meteorological Magazine*, *47*, 295–308.

Droplet Measurement Technologies, Inc. (n.d.). *Cloud, Aerosol, and Precipitation Spectrometer with Depolarization*. Retrieved July 22, 2024, from https://www.dropletmeasurement.com/product/cloud-aerosol-and-precipitation-spectrometer-with-depolarization/

Droplet Measurement Technologies, Inc. (2009). *Data Analysis User's Guide. Chapter I: Single Particle Light Scattering. DOC-0222, Rev A*.

Fan, C., He, B., Guo, S., Qiu, J., & Zhao, C. (2025). *Insights into the real part of natural sea spray aerosol refractive index in the Pacific Ocean*. https://doi.org/10.5194/egusphere-2024-3527

Feng, L., Shen, H., Zhu, Y., Gao, H., & Yao, X. (2017). Insight into Generation and Evolution of Sea-Salt Aerosols from Field Measurements in Diversified Marine and Coastal Atmospheres. *Scientific Reports*, *7*(1), 41260. https://doi.org/10.1038/srep41260

Flores, J. M., Bourdin, G., Kostinski, A. B., Altaratz, O., Dagan, G., Lombard, F., Haëntjens, N., Boss, E., Sullivan, M. B., Gorsky, G., Lang-Yona, N., Trainic, M., Romac, S., Voolstra, C. R., Rudich, Y., Vardi, A., & Koren, I. (2021). Diel cycle of sea spray aerosol concentration. *Nature Communications*, *12*(1), Article 1. https://doi.org/10.1038/s41467-021-25579-3

Forestieri, S. D., Moore, K. A., Martinez Borrero, R., Wang, A., Stokes, M. D., & Cappa, C. D. (2018). Temperature and Composition Dependence of Sea Spray Aerosol Production. *Geophysical Research Letters*, *45*(14), 7218–7225. https://doi.org/10.1029/2018GL078193

Froyd, K. D., Murphy, D. M., Brock, C. A., Campuzano-Jost, P., Dibb, J. E., Jimenez, J.-L., Kupc, A., Middlebrook, A. M., Schill, G. P., Thornhill, K. L., Williamson, C. J., Wilson,

J. C., & Ziemba, L. D. (2019). A new method to quantify mineral dust and other aerosol species from aircraft platforms using single-particle mass spectrometry. *Atmospheric Measurement Techniques*, *12*(11), 6209–6239. https://doi.org/10.5194/amt-12-6209-2019

Glen, A., & Brooks, S. D. (2013). A new method for measuring optical scattering properties of atmospherically relevant dusts using the Cloud and Aerosol Spectrometer with Polarization (CASPOL). *Atmospheric Chemistry and Physics*, *13*(3), 1345–1356. https://doi.org/10.5194/acp-13-1345-2013

Grini, A., Myhre, G., Sundet, J. K., & Isaksen, I. S. A. (2002). Modeling the Annual Cycle of Sea Salt in the Global 3D Model Oslo CTM2: Concentrations, Fluxes, and Radiative Impact. *Journal of Climate*, *15*(13), 1717–1730. https://doi.org/10.1175/1520-0442(2002)015<1717:MTACOS>2.0.CO;2

Grythe, H., Ström, J., Krejci, R., Quinn, P., & Stohl, A. (2014). A review of sea-spray aerosol source functions using a large global set of sea salt aerosol concentration measurements. *Atmospheric Chemistry and Physics*, *14*(3), 1277–1297. https://doi.org/10.5194/acp-14-1277-2014

Hinds, W. C. (1999). *Aerosol Technology: Properties, Behavior, and Measurement of Airborne Particles*. John Wiley & Sons, Incorporated. http://ebookcentral.proquest.com/lib/univie/detail.action?docID=1120423

Jaeglé, L., Quinn, P. K., Bates, T. S., Alexander, B., & Lin, J.-T. (2011). Global distribution of sea salt aerosols: New constraints from in situ and remote sensing observations. *Atmospheric Chemistry and Physics*, *11*(7), 3137–3157. https://doi.org/10.5194/acp-11-3137-2011

Kalová, J., & Mareš, R. (2015). Reference Values of Surface Tension of Water. *International Journal of Thermophysics*, *36*(7), 1396–1404. https://doi.org/10.1007/s10765-015-1907-2

Koch, D., Schmidt, G. A., & Field, C. V. (2006). Sulfur, sea salt, and radionuclide aerosols in GISS ModelE. *Journal of Geophysical Research: Atmospheres*, *111*(D6). https://doi.org/10.1029/2004JD005550

Lewis, E. R., & Schwartz, S. E. (2004). *Sea salt aerosol production: Mechanisms, methods, measurements, and models* (Vol. 152). American geophysical union.

Liao, H., Seinfeld, J. H., Adams, P. J., & Mickley, L. J. (2004). Global radiative forcing of coupled tropospheric ozone and aerosols in a unified general circulation model. *Journal of Geophysical Research: Atmospheres*, *109*(D16). https://doi.org/10.1029/2003JD004456

Linstrom, P. J., & Mallard, W. G. (Eds.). (n.d.). *NIST Chemistry WebBook, NIST Standard Reference Database Number 69* (20899th ed.). National Institute of Standards and Technology. https://doi.org/10.18434/T4D303

Liu, S., Liu, C.-C., Froyd, K. D., Schill, G. P., Murphy, D. M., Bui, T. P., Dean-Day, J. M., Weinzierl, B., Dollner, M., Diskin, G. S., Chen, G., & Gao, R.-S. (2021). Sea spray aerosol concentration modulated by sea surface temperature. *Proceedings of the National Academy of Sciences*, *118*(9), e2020583118. https://doi.org/10.1073/pnas.2020583118

Lohmann, U., Lüönd, F., & Mahrt, F. (2016). *An Introduction to Clouds: From the Microscale to Climate*. Cambridge University Press. https://doi.org/10.1017/CBO9781139087513

Ma, X., von Salzen, K., & Li, J. (2008). Modelling sea salt aerosol and its direct and indirect effects on climate. *Atmospheric Chemistry and Physics*, *8*(5), 1311–1327. https://doi.org/10.5194/acp-8-1311-2008

Mårtensson, E. M., Nilsson, E. D., de Leeuw, G., Cohen, L. H., & Hansson, H.-C. (2003). Laboratory simulations and parameterization of the primary marine aerosol production. *Journal of Geophysical Research: Atmospheres*, *108*(D9). https://doi.org/10.1029/2002JD002263

Meteorological Measurement System. (n.d.). NASA Airborne Science Program. Retrieved August 13, 2024, from https://airbornescience.nasa.gov/mms

Metropolis, N., & Ulam, S. (1949). The Monte Carlo Method. *Journal of the American Statistical Association*, *44*(247), 335–341. https://doi.org/10.1080/01621459.1949.10483310

Modini, R. L., Russell, L. M., Deane, G. B., & Stokes, M. D. (2013). Effect of soluble surfactant on bubble persistence and bubble-produced aerosol particles. *Journal of Geophysical Research: Atmospheres*, *118*(3), 1388–1400. https://doi.org/10.1002/jgrd.50186

MODIS Science Team. (2021a). *MODIS/Aqua Thermal Anomalies/Fire 5-Min L2 Swath 1km NRT* [Dataset]. NASA LANCE MODIS at the MODAPS. https://doi.org/10.5067/MODIS/MYD14.NRT.061

MODIS Science Team. (2021b). *MODIS/Terra Thermal Anomalies/Fire 5-Min L2 Swath 1km NRT* [Dataset]. NASA LANCE MODIS at the MODAPS. https://doi.org/10.5067/MODIS/MOD14.NRT.061

Murphy, D. M., Cziczo, D. J., Froyd, K. D., Hudson, P. K., Matthew, B. M., Middlebrook, A. M., Peltier, R. E., Sullivan, A., Thomson, D. S., & Weber, R. J. (2006). Single-particle mass spectrometry of tropospheric aerosol particles. *Journal of Geophysical Research: Atmospheres*, *111*(D23). https://doi.org/10.1029/2006JD007340

Murphy, D. M., Froyd, K. D., Bian, H., Brock, C. A., Dibb, J. E., DiGangi, J. P., Diskin, G., Dollner, M., Kupc, A., Scheuer, E. M., Schill, G. P., Weinzierl, B., Williamson, C. J., & Yu, P. (2019). The distribution of sea-salt aerosol in the global troposphere. *Atmospheric Chemistry and Physics*, *19*(6), 4093–4104. https://doi.org/10.5194/acp-19-4093-2019

Myhre, G., Shindell, D., Bréon, F.-M., Collins, W., Fuglestvedt, J., Huang, J., Koch, D., Lamarque, J.-F., Lee, D., Mendoza, B., Nakajima, T., Robock, A., Stephens, G., Takemura, T., & Zhang, H. (2013). Anthropogenic and Natural Radiative Forcing. In *Climate Change 2013: The Physical Science Basis. Contribution of Working Group I to*

the Fifth Assessment Report of the Intergovernmental Panel on Climate Change (Stocker, T.F., D. Qin, G.-K. Plattner, M. Tignor, S.K. Allen, J. Boschung, A. Nauels, Y. Xia, V. Bex and P.M. Midgley (eds.)). Cambridge University Press.

NASA VIIRS Land Science Team. (2020a). *VIIRS (NOAA-20/JPSS-1) I Band 375 m Active Fire Product NRT (Vector data)* [Dataset]. NASA LANCE MODIS at the MODAPS. https://doi.org/10.5067/FIRMS/VIIRS/VJ114IMGT_NRT.002

NASA VIIRS Land Science Team. (2020b). *VIIRS/NPP Active Fires 6-Min L2 Swath 375m NRT* [Dataset]. NASA LANCE MODIS at the MODAPS. https://doi.org/10.5067/VIIRS/VNP14IMG_NRT.002

O'Dowd, C. D., Facchini, M. C., Cavalli, F., Ceburnis, D., Mircea, M., Decesari, S., Fuzzi, S., Yoon, Y. J., & Putaud, J.-P. (2004). Biogenically driven organic contribution to marine aerosol. *Nature*, *431*(7009), 676–680. https://doi.org/10.1038/nature02959

O'Dowd, C. D., & Smith, M. H. (1993). Physicochemical properties of aerosols over the northeast Atlantic: Evidence for wind-speed-related submicron sea-salt aerosol production. *Journal of Geophysical Research: Atmospheres*, *98*(D1), 1137–1149. https://doi.org/10.1029/92JD02302

Pant, V., Deshpande, C. G., & Kamra, A. K. (2008). On the aerosol number concentration–wind speed relationship during a severe cyclonic storm over south Indian Ocean. *Journal of Geophysical Research: Atmospheres*, *113*(D2). https://doi.org/10.1029/2006JD008035

Petters, M. D., & Kreidenweis, S. M. (2007). A single parameter representation of hygroscopic growth and cloud condensation nucleus activity. *Atmospheric Chemistry and Physics*, *7*(8), 1961–1971. https://doi.org/10.5194/acp-7-1961-2007

Reddy, M. S., Boucher, O., Balkanski, Y., & Schulz, M. (2005). Aerosol optical depths and direct radiative perturbations by species and source type. *Geophysical Research Letters*, *32*(12). https://doi.org/10.1029/2004GL021743

Rolph, G., Stein, A., & Stunder, B. (2017). Real-time Environmental Applications and Display sYstem: READY. *Environmental Modelling & Software*, *95*, 210–228. https://doi.org/10.1016/j.envsoft.2017.06.025

Saliba, G., Chen, C.-L., Lewis, S., Russell, L. M., Rivellini, L.-H., Lee, A. K. Y., Quinn, P. K., Bates, T. S., Haëntjens, N., Boss, E. S., Karp-Boss, L., Baetge, N., Carlson, C. A., & Behrenfeld, M. J. (2019). Factors driving the seasonal and hourly variability of sea-spray aerosol number in the North Atlantic. *Proceedings of the National Academy of Sciences*, *116*(41), 20309–20314. https://doi.org/10.1073/pnas.1907574116

Scott, S. G., Bui, T. P., Chan, K. R., & Bowen, S. W. (1990). *The Meteorological Measurement System on the NASA ER-2 Aircraft*. https://journals.ametsoc.org/view/journals/atot/7/4/1520-0426_1990_007_0525_tmmsot_2_0_co_2.xml

Seinfeld, J. H., & Pandis, S. N. (1998). *Atmospheric Chemistry and Physics: From Air Pollution to Climate Change*. Wiley.

Shinozuka, Y., Clarke, A. D., Howell, S. G., Kapustin, V. N., & Huebert, B. J. (2004). Sea-salt vertical profiles over the Southern and tropical Pacific oceans: Microphysics, optical properties, spatial variability, and variations with wind speed. *Journal of Geophysical Research: Atmospheres*, *109*(D24). https://doi.org/10.1029/2004JD004975

Simpson, W. R., Brown, S. S., Saiz-Lopez, A., Thornton, J. A., & von Glasow, R. (2015). Tropospheric Halogen Chemistry: Sources, Cycling, and Impacts. *Chemical Reviews*, *115*(10), 4035–4062. https://doi.org/10.1021/cr5006638

Springston, S., Trojanowski, R., & Hayes, C. (2025). *CO/H2O/N2O Analyzer Instrument Handbook*. U.S. Department of Energy, Atmospheric Radiation Measurement user facility.

Stein, A. F., Draxler, R. R., Rolph, G. D., Stunder, B. J. B., Cohen, M. D., & Ngan, F. (2015). *NOAA's HYSPLIT Atmospheric Transport and Dispersion Modeling System*. https://doi.org/10.1175/BAMS-D-14-00110.1

Stull, R. (1988). *An introduction to boundary layer meteorology*.

Stull, R. (2006). 9—The Atmospheric Boundary Layer. In J. M. Wallace & P. V. Hobbs (Eds.), *Atmospheric Science (Second Edition)* (pp. 375–417). Academic Press. https://doi.org/10.1016/B978-0-12-732951-2.50014-4

Tang, I. N., Tridico, A. C., & Fung, K. H. (1997). Thermodynamic and optical properties of sea salt aerosols. *Journal of Geophysical Research: Atmospheres*, *102*(D19), 23269–23275. https://doi.org/10.1029/97JD01806

Tiesinga, E., Mohr, P. J., Newell, D. B., & Taylor, B. N. (2021). CODATA recommended values of the fundamental physical constants: 2018. *Reviews of Modern Physics*, *93*(2), 025010. https://doi.org/10.1103/RevModPhys.93.025010

Tobin, D. C., Revercomb, H. E., Knuteson, R. O., Best, F. A., Smith, W. L., Ciganovich, N. N., Dedecker, R. G., Dutcher, S., Ellington, S. D., Garcia, R. K., Howell, H. B., LaPorte, D. D., Mango, S. A., Pagano, T. S., Taylor, J. K., van Delst, P., Vinson, K. H., & Werner, M. W. (2006). Radiometric and spectral validation of Atmospheric Infrared Sounder observations with the aircraft-based Scanning High-Resolution Interferometer Sounder. *Journal of Geophysical Research: Atmospheres*, *111*(D9). https://doi.org/10.1029/2005JD006094

Veron, F. (2015). Ocean Spray. *Annual Review of Fluid Mechanics*, *47*(Volume 47, 2015), 507–538. https://doi.org/10.1146/annurev-fluid-010814-014651

Winter, B., & Chýlek, P. (1997). *Contribution of sea salt aerosol to the planetary clear-sky albedo* (1). *49*(1), Article 1. https://doi.org/10.3402/tellusb.v49i1.15951

Zábori, J., Krejci, R., Ekman, A. M. L., Mårtensson, E. M., Ström, J., de Leeuw, G., & Nilsson, E. D. (2012). Wintertime Arctic Ocean sea water properties and primary marine aerosol concentrations. *Atmospheric Chemistry and Physics*, *12*(21), 10405–10421. https://doi.org/10.5194/acp-12-10405-2012

Zha, J., Shen, C., Li, Z., Wu, J., Zhao, D., Fan, W., Sun, M., Azorin-Molina, C., & Deng, K. (2021). Projected changes in global terrestrial near-surface wind speed in 1.5 °C–4.0 °C global warming levels. *Environmental Research Letters*, *16*(11), 114016. https://doi.org/10.1088/1748-9326/ac2fdd

Zheng, G., Wang, Y., Aiken, A. C., Gallo, F., Jensen, M. P., Kollias, P., Kuang, C., Luke, E., Springston, S., Uin, J., Wood, R., & Wang, J. (2018). Marine boundary layer aerosol in the eastern North Atlantic: Seasonal variations and key controlling processes. *Atmospheric Chemistry and Physics*, *18*(23), 17615–17635. https://doi.org/10.5194/acp-18-17615-2018

Zhu, L., Jacob, D. J., Eastham, S. D., Sulprizio, M. P., Wang, X., Sherwen, T., Evans, M. J., Chen, Q., Alexander, B., Koenig, T. K., Volkamer, R., Huey, L. G., Le Breton, M., Bannan, T. J., & Percival, C. J. (2019). Effect of sea salt aerosol on tropospheric bromine chemistry. *Atmospheric Chemistry and Physics*, *19*(9), 6497–6507. https://doi.org/10.5194/acp-19-6497-2019

Appendix

Size-resolved Aerosol Composition

Table A.1 Size-resolved composition of aerosol measured during the periods of interest of flight 20230616.

	Size Range		
	0.5 – 1 µm	**1 – 1.5 µm**	**1.5 – 4 µm**
Number fraction [%]			
Sea Salt	25	79	93
Biomass Burning	10	7	0
Sulfate/Organic/Nitrate	62	10	1
Dust	0	1	3
Alkali	0	0	0
Soot	0	0	0
Meteoric	0	0	0
Vanadium	1	1	0
Unclassified	2	2	2

Table A.2 Size-resolved composition of aerosol measured during during the periods of interest of flight 20230619.

	Size Range		
	0.5 – 1 µm	**1 – 1.5 µm**	**1.5 – 4 µm**
Number fraction [%]			
Sea Salt	16	73	89
Biomass Burning	17	6	0
Sulfate/Organic/Nitrate	63	16	2
Dust	0	2	4
Alkali	0	0	0
Soot	0	0	0
Meteoric	1	1	0
Vanadium	2	1	0
Unclassified	1	1	4

Table A.3 Size-resolved composition of aerosol measured during during the periods of interest of flight 20230621.

	Size Range			
Number fraction [%]		0.5 – 1 µm	1 – 1.5 µm	1.5 – 4 µm
	Sea Salt	7	56	89.41
	Biomass Burning	30	30	1.31
	Sulfate/Organic/Nitrate	60	11	1.93
	Dust	0	0	3.88
	Alkali	0	0	0.49
	Soot	0	0	0.32
	Meteoric	0	0	0.05
	Vanadium	0	0	0.10
	Unclassified	2	3	2.52

Table A.4 Size-resolved composition of aerosol measured during during the periods of interest of flight 20230623.

	Size Range			
Number fraction [%]		0.5 – 1 µm	1 – 1.5 µm	1.5 – 4 µm
	Sea Salt	10	89	88
	Biomass Burning	42	6	3
	Sulfate/Organic/Nitrate	40	3	3
	Dust	0	0	3
	Alkali	0	0	0
	Soot	0	0	0
	Meteoric	0	0	0
	Vanadium	1	0	0
	Unclassified	6	1	2

Timeseries including CO, DMS and jNO2

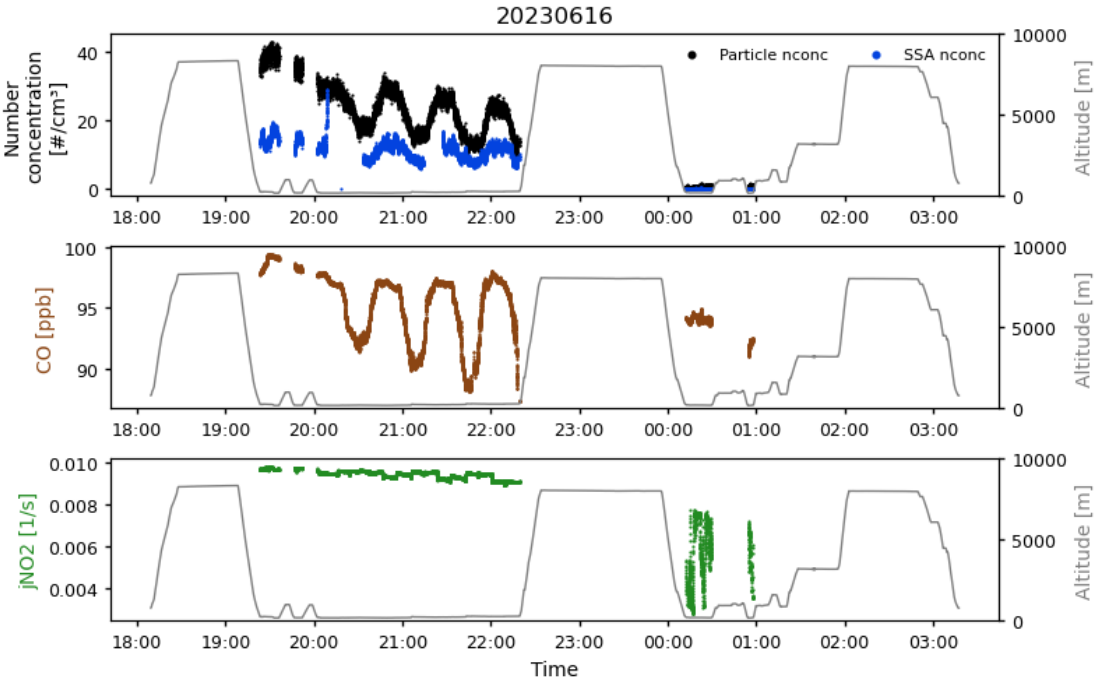

Figure A.1: Timeseries of flight 20230616. The upper plot shows particle number concentration, SSA number concentration and the altitude profile. The middle plot shows CO mixing ratio and the altitude profile. The bottom plot shows NO2 reactivity rate and the altitude profile. For all plots, the altitude profile is shown for the entire flight, other data is only plotted for periods of interest

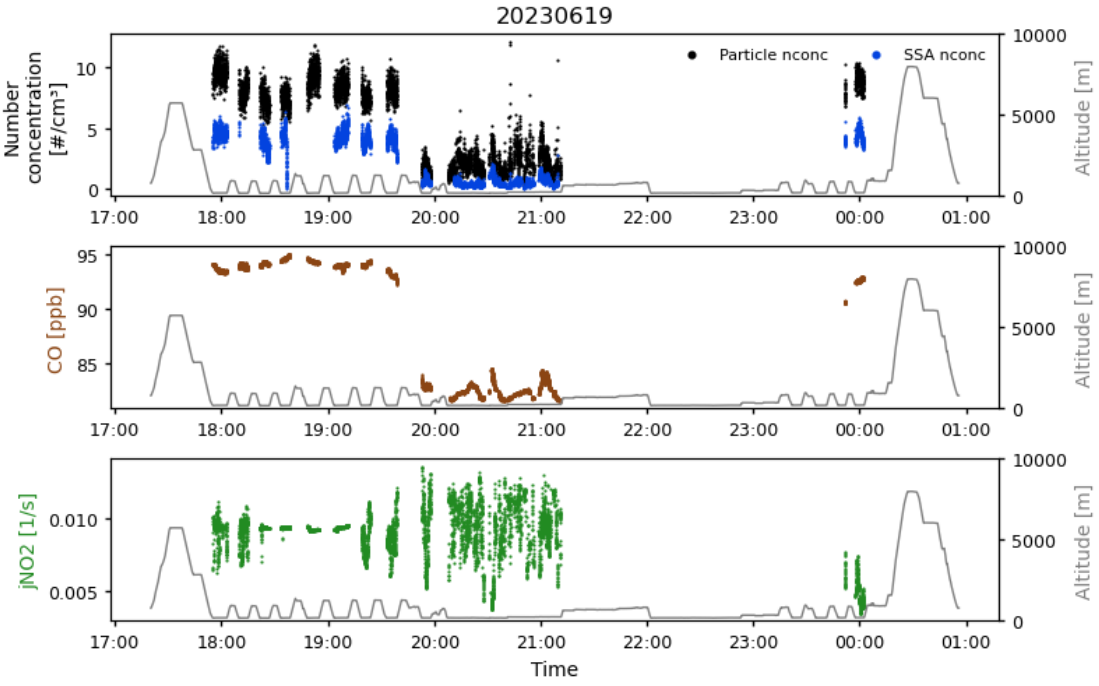

Figure A.2: Timeseries of flight 20230616. The upper plot shows particle number concentration, SSA number concentration and the altitude profile. The middle plot shows CO mixing ratio and the altitude profile. The bottom plot shows NO2 reactivity rate and the altitude profile. For all plots, the altitude profile is shown for the entire flight, other data is only plotted for periods of interest.

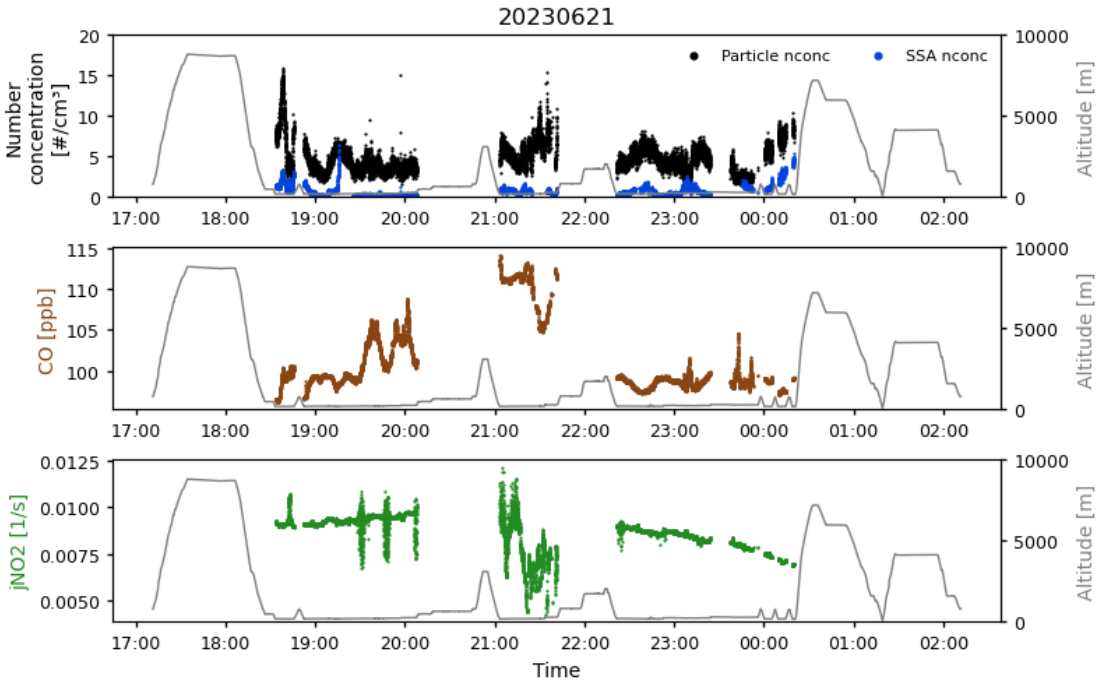

Figure A.3: Timeseries of flight 20230616. The upper plot shows particle number concentration, SSA number concentration and the altitude profile. The middle plot shows CO mixing ratio and the altitude profile. The bottom plot shows NO2 reactivity rate and the altitude profile. For all plots, the altitude profile is shown for the entire flight, other data is only plotted for periods of interest.

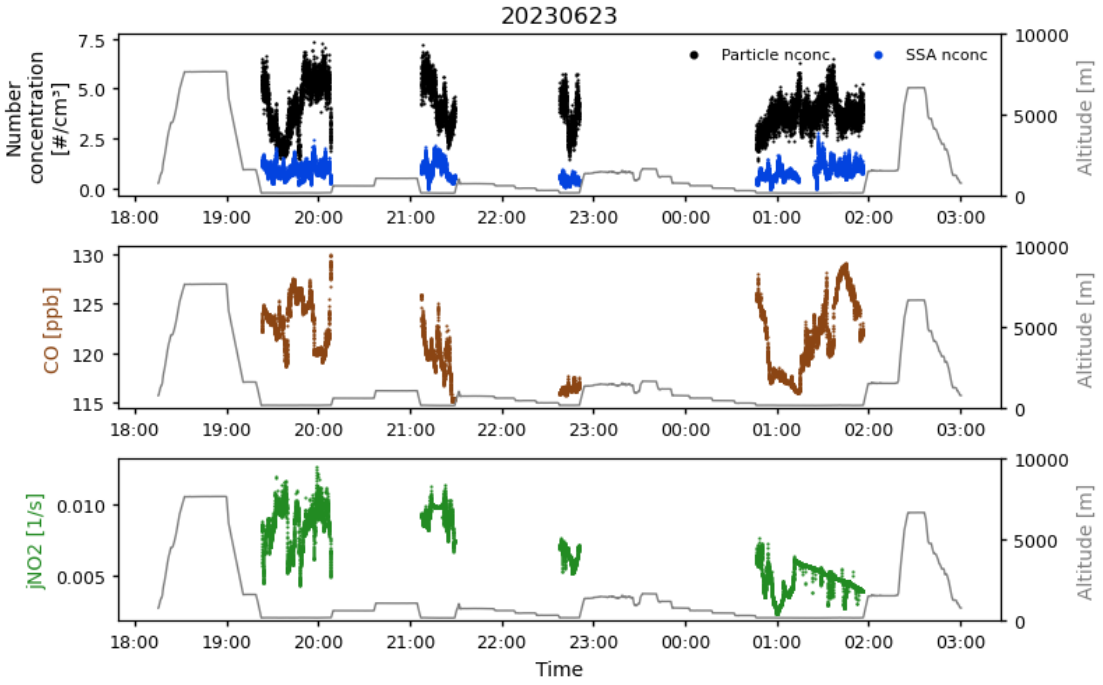

Figure A.4: Timeseries of flight 20230616. The upper plot shows particle number concentration, SSA number concentration and the altitude profile. The middle plot shows CO mixing ratio and the altitude profile. The bottom plot shows NO2 reactivity rate and the altitude profile. For all plots, the altitude profile is shown for the entire flight, other data is only plotted for periods of interest

HYSPLIT trajectories

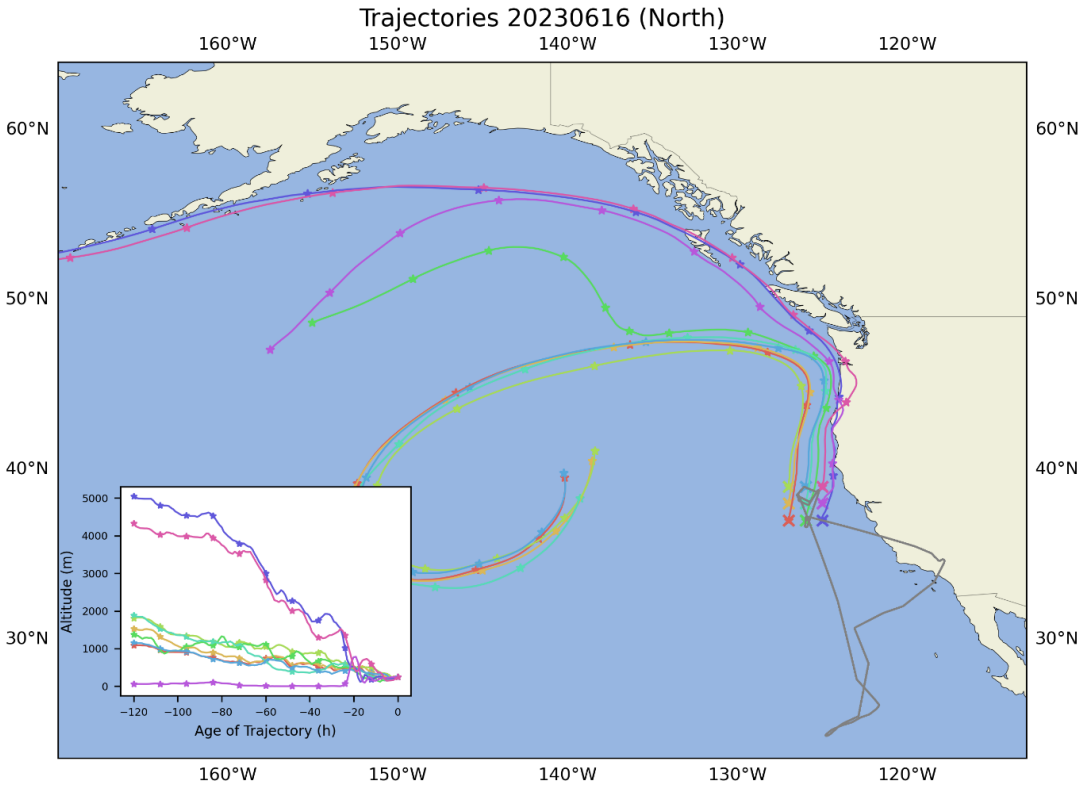

Figure A.5: HYSPLIT back trajectories of flight 20230616 (northern region).

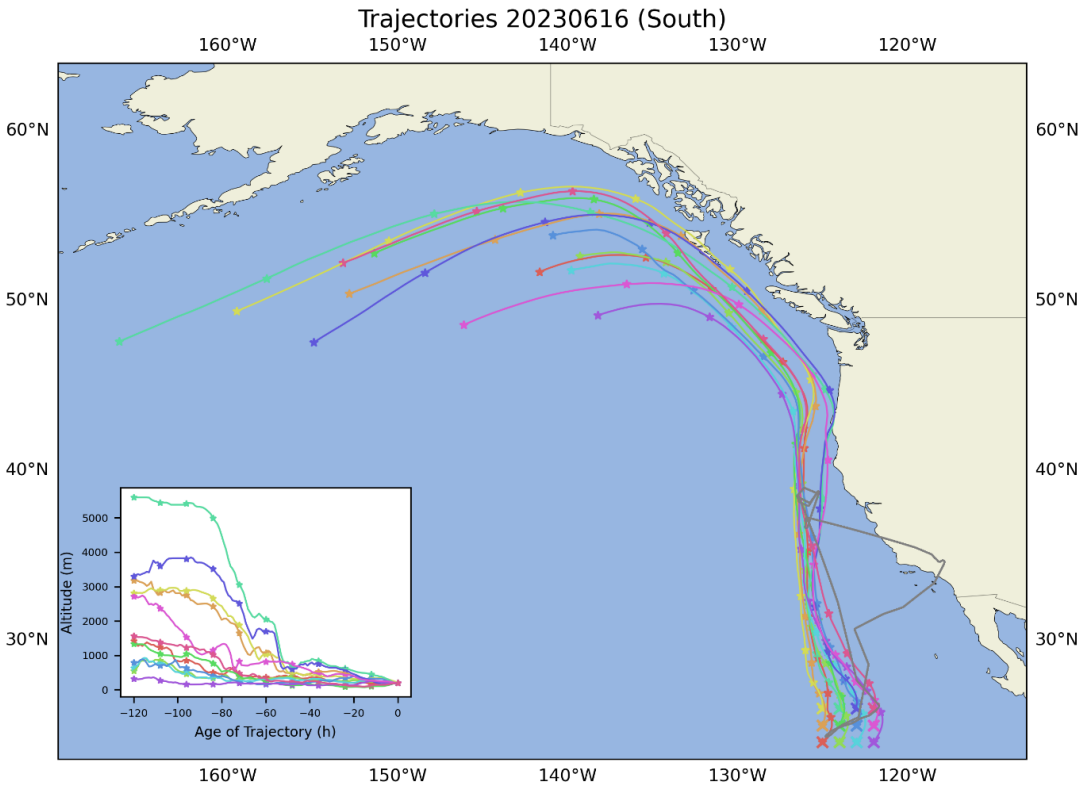

Figure A.6: HYSPLIT back trajectories of flight 20230616 (southern region).

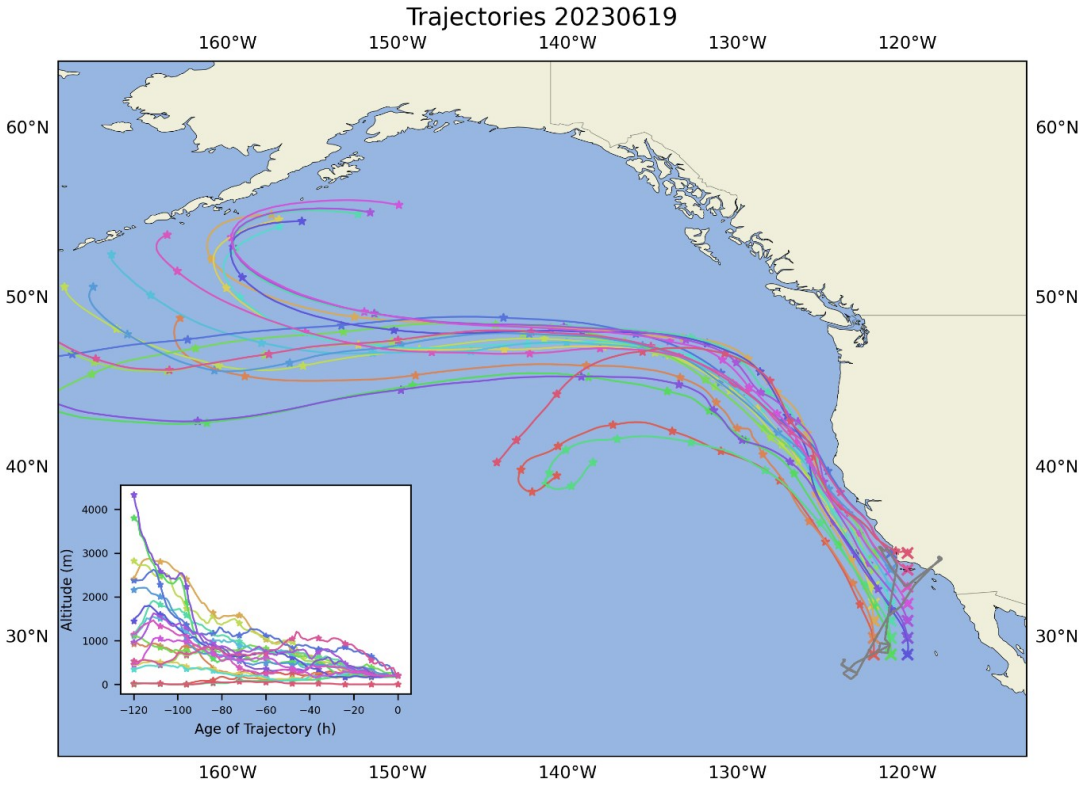

Figure A.7: HYSPLIT back trajectories of flight 20230619.

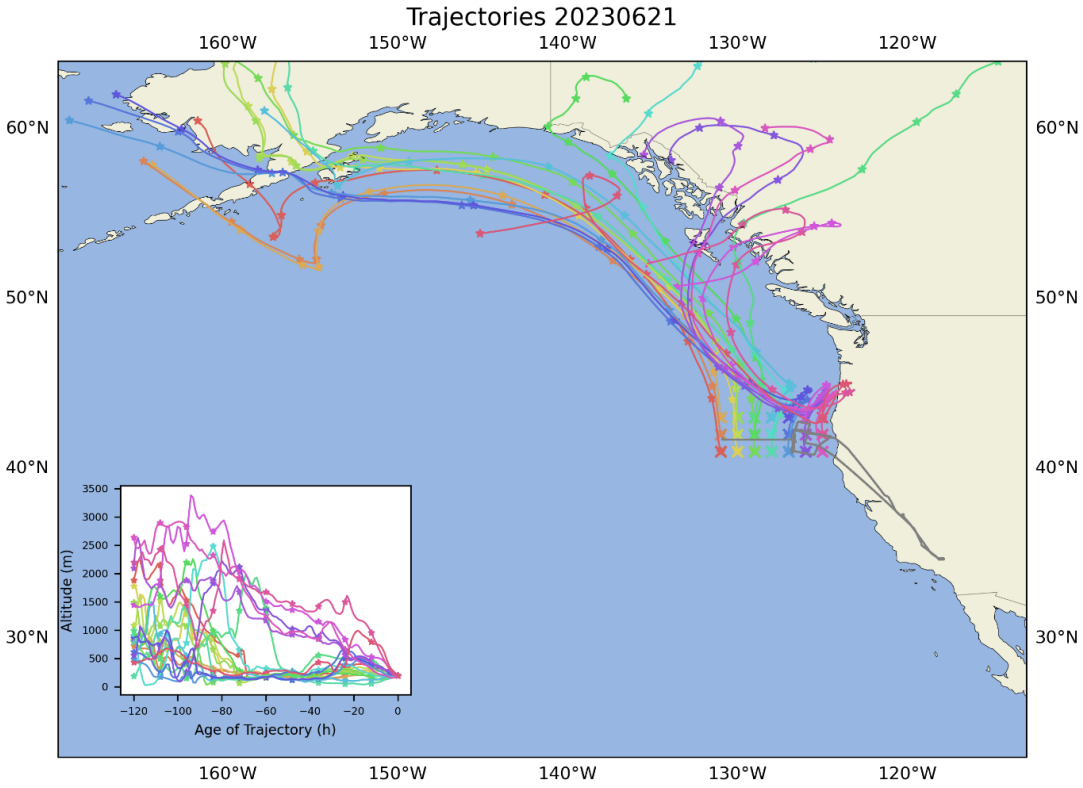

Figure A.8: HYSPLIT back trajectories of flight 20230621.

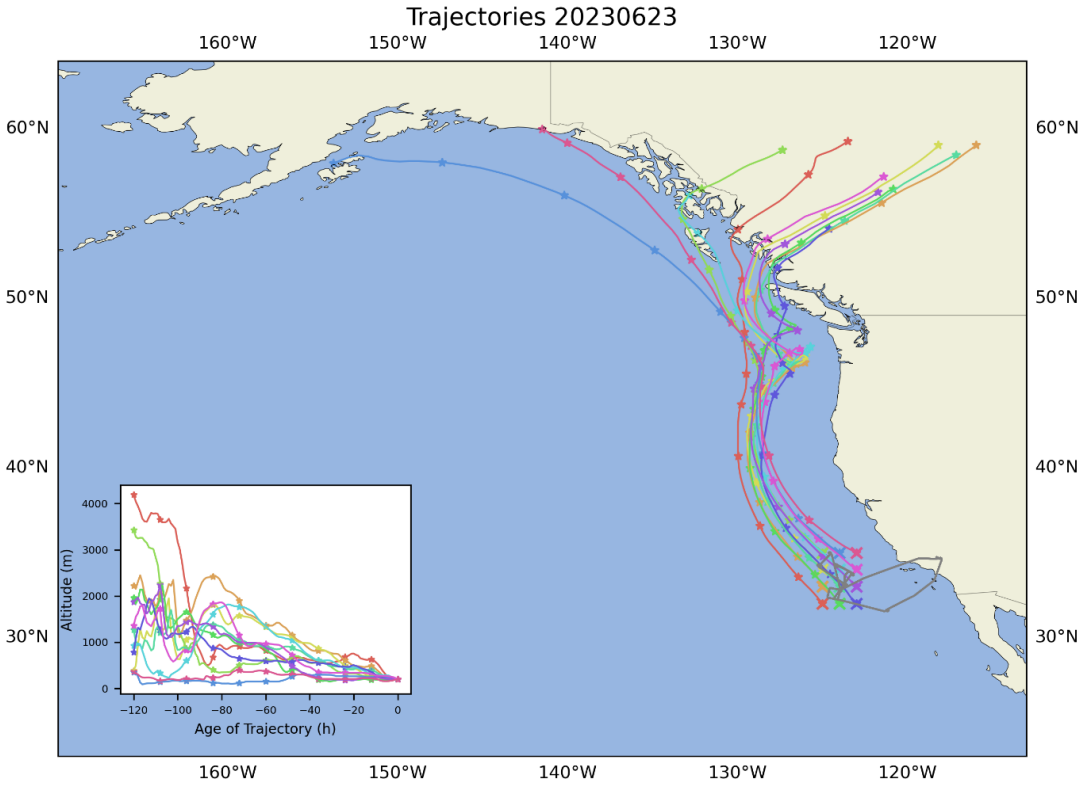

Figure A.9: HYSPLIT back trajectories of flight 20230623.